scientific reports

Check for updates

OPEN

Numerical and machine learning framework for strategic fin design to accelerate phase change material melting in advanced enclosures

M. Ramanipriya[1], Iskander Tlili[2]✉ & S. Anitha[1]

The melting behavior of phase change materials (PCMs) is numerically investigated in rectangular, trapezoidal, and heptahedral enclosures equipped with identical V-shaped fins, under coupled parametric variations. The investigated parameters include PCM type (RT-25 to RT-38), fin material (aluminum, copper, steel), fin inclination angle (30°–90°), and heat flux (500–2000 W/m^2). The transient melting process is simulated using the enthalpy-based method, emphasizing the conduction-to-convection transition during early-stage melting dynamics. RT-25 exhibits the fastest melting (complete melting within 1500 s), while RT-27 shows the slowest behavior (liquid fraction of 0.172 after 1500 s). Aluminum provides a 27.6% higher average heat transfer coefficient compared to steel. The heptahedral enclosure achieves a 34.9% higher liquid fraction and 20.4% reduction in melting time compared to the rectangular configuration. Fin inclination angles between 70° and 90° yield the highest melting rates. Increasing heat flux from 500 to 2000 W/m^2 reduces the Fourier number for complete melting by 77.56%. A Random Forest regression model predicts the Nusselt number with R^2 values of 0.9896 (training) and 0.9729 (testing), with MAPE of 2.74% and 3.68%. SHAP analysis reveals that extreme heat flux conditions (500 and 2000 W/m^2) exert the greatest influence on predictions. The novelty lies in the systematic investigation of coupled geometric, material, and operational parameters, providing the first comparative assessment of these three enclosures with identical V-shaped fins. The findings establish practical design guidelines for selecting PCM-fin configurations in latent heat thermal energy storage systems, demonstrating that the combination of heptahedral enclosure, aluminum fins, and near-vertical inclination (70°–90°) provides the most effective thermal performance.

Keywords Heptahedron enclosure, Phase change material, Melting properties, Heat flux, Nusselt number, Random forests

List of symbols

Abbreviations

HTC	Heat transfer coefficient
LF	Liquid fraction
MAE	Mean absolute error
ML	Machine learning
MSE	Mean squared error
Nu	Nusselt number
PCM	Phase change material
RF	Random forests
RMSE	Root mean squared error
RT	RubiTherm

[1]Department of Mathematics, PSG Institute of Technology and Applied Research, Coimbatore, Tamil Nadu, India. [2]Department of Mechanical Engineering, Faculty of Engineering, Islamic University of Madinah, Madinah, Saudi Arabia. ✉email: itlili@iu.edu.sa

SHAP	SHapley Additive exPLanations

Symbols

A_{mush}	Mushy zone constant (kg/m^{3}s)
C_p	Specific heat (kJ/kg K)
Fo	Fourier number (–)
$\overrightarrow{g}$	Gravitational acceleration (m/s^2)
H	Total enthalpy (kJ/kg)
ΔH	Latent heat (kJ/kg)
k	Thermal conductivity (W/mK)
L_h	Latent heat of fusion (kJ/kg)
P	Pressure (Pa)
Q	Heat flux (W/m^2)
$\overrightarrow{S}$	Source term (–)
T	Temperature (°C)
T_l	Liquids temperature (°C)
T_m	Melting temperature (°C)
T_s	Solidus temperature (°C)
$\overrightarrow{v}$	Velocity vector (m/s)

Greek letters

α	Inclination angle (degrees)
β	Thermal expansion (1/K)
γ	Liquid fraction (–)
ε	Small number (=0.0001) (–)
μ	Dynamic viscosity (kg/ms)
ρ	Density (kg/m^3)

Phase change materials (PCMs) work by absorbing or releasing energy as they change phase, and this process can deliver either heating or cooling effects. PCMs are typically categorized into organic materials and salt hydrates. The largest market for PCMs is in building heating and cooling, driven by the rising cost of renewable electricity and the challenges of intermittent peak demand. PCMs have a wide range of applications, including thermal energy storage, cold-energy battery conditioning, waste heat recovery, and reducing both power consumption and reliance on diesel generators. Dinghai Liu and Kai Xie [1] investigated the flow and heat transfer behaviour of a phase change material (PCM) within a rotating, paraffin-filled rectangular container in space. They employed a three-dimensional computational model and the enthalpy method to simulate the melting process and fluid dynamics at the solid–liquid interface. The results showed that the peak natural convection velocity increased with both radial height and melting time. Hua-Yang Liu et al. [2] proposed a heptahedral thermal energy system engineered for better natural convection and reduce melting time. The enclosure's volume distribution and length ratio are found to significantly affect the melting behavior of the RT-42 PCM. The heptahedral structure prolongs dominant melting stage, improves natural convection, and reduces the thermal resistance of the PCM. Phase-change materials (PCMs) are essential to thermal energy storage by balancing energy supply and demand. However, their performance is strongly influenced by melting and solidification behavior, based on the position of the heat source and geometric configuration of the system. Results indicate that side heating accelerates the melting process especially in circular enclosures while top heating is less effective in promoting phase change [3].

Further research is explored the effect of boundary conditions, complex geometries, and different PCM materials with unique thermal properties. Take numerical simulations as an example. Researchers used them to look at the melting process of RT-42 when irregular longitudinal fins are placed near the bottom of a heated sidewall enclosure [4]. A study focused on boosting natural convection, particularly during the final stage of melting. Fins placed in the lower region gave the best performance. The melting behavior of a PCM in a rectangular container heated from the bottom surface is analyzed, with a focus on the effect of fin spacing using aluminium and stainless-steel fin materials. The optimal fin length is found to vary depending on the material and fin pitch [5]. Rejane De Cesaro Oliveski et al. [6] analyzed the melting process of lauric acid PCM in a finned rectangular cavity, focusing on fin aspect ratios. The study suggested that additional fin configurations and varying temperature differences could be further investigated. It is also observed that adding copper fins to a square cell containing paraffin wax (RT-42 PCM) significantly improved the charging rate. The addition of fins reduced the melting time of the wax by 22.22%, 33.33%, and 55.56% in contrast with the configuration lacking fins. The wall with fins provided the optimal surface for heat flux application, indicating that placing fins on the left wall offered the best efficiency [7]. The behavior of rectangular fins inside a square cavity is examined, focusing on heat transfer and fluid flow. Both inverse CFD and experimental analysis are used to carry out the investigation. A heat sink with paraffin PCM is proposed, revealing that a PCM heat sink with reduced height enhanced heat dissipation efficiency, absorbing 22.5% more thermal energy [8]. Fin arrangements are further explored as a means to improve the thermal performance of latent heat storage units. Fin distribution optimization and transient melting behavior of n-octadecane are predicted using the enthalpy–porosity approach. The results showed that heat transfer performance and melting behavior are greatly influenced by fin structures [9].

A numerical study investigated the melting of PCM in triangular cylindrical containers using paraffin wax and hot air. It examined flow structure and convective heat transfer while assessing heat storage capacity for different container geometries. It is found that the apex angle and base length of the triangle significantly affect the container's surface temperature and overall heat storage effectiveness [10]. Yuxiang Hong and Yuan Shi [11] proposed a method for enhancing latent heat energy storage units by combining T-shaped fins with divided subzones. Their results showed that the fin structure and PCM layout have a significant impact on melting

performance. T-shaped fins reduced the melting process duration by up to 68.5% and increased the average integral heat transfer rate by up to 257.4%. The usage of a latent heat thermal energy storage (LHTES) unit integrated with solar receivers or photovoltaic thermal management systems is also studied. The impact of eight different T-fin positions on thermal performance of PCM is analyzed. Results indicated that the PCM melting rate is highly influenced by fin placement, with top-mounted fins giving the highest improvement [12].

Recent studies have investigated cyclic heating and cooling strategies to improve PCM performance, reducing melting time and enhancing energy storage capacity. Enhanced cyclic heating cooling techniques combined with optimized fin designs offer a promising solution [13]. The impact of partition types on phase-change duration in thermal energy storage systems has also been investigated. Vertical tubes and horizontal partitions gave the shortest melting and solidification times. It concluded that the thermal conductivity of partitions contributes to a more homogeneous temperature distribution, thereby facilitating uniform heat flux extraction and supply [14]. A numerical investigation evaluated the melting characteristics of PCM in rectangular encapsulations with various fin shape configurations. While straight fins are commonly used to enhance heat transfer, an excessive number of fins can hinder natural convection effects. Results showed that altering fin shapes improved the overall melting performance [15].

Zhenxing Zhao et al. [16] analyzed two-phase flow boiling behavior in channels with staggered pin fins using the Mixture multiphase model. The impacts of fin cross-sectional shape on heat transfer, pressure drop, and temperature uniformity under varying heat fluxes is examined. Results indicated that the pentagonal finned channel provided the best overall performance, making it the most efficient design. The influence of an air layer on paraffin wax (RT-42) melting within a hemicylindrical enclosure is also investigated. Three scenarios are considered, each with different air layer thicknesses. Results showed that adding a 1 mm thick air layer extended the complete melting time by 125%, while a 2 mm thick layer increased it by 225% [17].

The behavior of a PCM-based latent thermal energy storage (LTES) system during melting is investigated within a two-dimensional rectangular enclosure. Transient two-dimensional numerical simulations are carried out to model PCM melting while accounting for natural convection. Results show that triangular and Y-fin enclosures delay melting more than rectangular fins. Among all the designs, the Y-fin configurations performed the best. The versions with equal and increasing steps delivered the highest time enhancement ratios and also showed larger average suppression ratios [18]. The usage of flanged fins to enhance the PCM melting process in a rectangular container is also analyzed. Different scenarios are examined based on the material and fin length ratio, using copper, aluminium, and carbon steel as fin materials. The results show that low Lu/Ld ratios combined with high thermal conductivity led to higher PCM melting rates. Copper fins outperform the other cases and are further optimized based on the flange to web ratio and Lu/Ld ratio [19]. Although phase change materials (PCMs) are essential for energy storage and heat transfer applications, their low thermal conductivity often suppresses heat transfer. To overcome this limitation, fins shaped like alphabets can be employed to improve heat transmission in PCM systems. The use of "L," "T," and "Y" shaped fins has been investigated, revealing significant improvements in heat transfer efficiency, thermal performance, and melting time. These findings provide perspectives on the potential of novel fin designs for more effective and sustainable thermal energy storage systems [20].

With machine learning, it can really boost both the performance and the design of PCM systems. It helps forecast thermal behavior, choose suitable materials, optimize the overall setup, and enable real-time control. By training these models on lab data or computer simulations, they learn to dynamically adjust key settings to maximize efficiency and performance. Suping Shen et al. [21] presented a new method for forecasting the dynamic melting behavior of PCM in a rectangle chamber with dual fins using an artificial neural network (ANN). An organized dataset for training the ANN model is generated through numerical simulations with three different fin lengths. Its accuracy in forecasting PCM melting under conditions outside the training data highlights its potential for thermal management system engineering. Machine learning (ML) predictive models have also been applied to predict the liquid fraction (LF) in building-integrated photovoltaic (PV) systems. Four configurations are proposed, and the auto-regressive integrated moving average (ARIMA) model outperformed the others. The ARIMA model achieved the shortest time to reach the desired LF value, demonstrating the potential of machine learning for efficient and sustainable energy solutions [22].

Another study analyzed heat exchange processes and phase transition characteristics of lauric acid in various PCM container designs during the liquefaction stage. According to the findings, rectangular-shaped containers had the slowest phase transition time but offered the best thermal energy retention, while tilting the containers led to faster melting. Combining artificial intelligence-driven simulations with container shape refinement is shown to improve both thermal performance and cost-effectiveness [23]. The impact of container position on the melting process of PCM in thermal energy storage systems is analyzed using computational fluid dynamics (CFD). It investigates effects of Reynolds numbers and H/D ratios on PCM melting. The XGBoost algorithm is applied for regression analysis, achieving a maximum accuracy of 99.35% and a minimum accuracy of 97.89% across 12 datasets [24]. The impacts of wave amplitude, fin length, and thickness on the fluid and thermal flow fields of thermal energy storage systems are also examined. Corrugated fins are shown to accelerate melting by increasing the heat transfer surface area and penetration depth. Longer and thicker fins enhance thermal energy storage capacity, average temperature, and melting rate. Furthermore, an artificial neural network combined with a particle swarm optimization model is used to optimize fin geometry, resulting in a 43% improvement in TES per unit mass [25].

Therefore, a parametric study is presented using three enclosure designs (rectangular, trapezoidal, and heptahedral) to examine the initial phase of the melting process. This study highlights the transition from primarily conductive to convective heat transfer. Bridging the gap between numerical and experimental validation studies is essential for improving the accuracy and reliability of prediction models. Researchers have explored finned designs in quite a few studies. But there is still a need for systematic optimization to figure out

the role that PCM type, inclination angle, cavity shape, and fin material play in making them effective. The novelty of the present work lies in the simultaneous and systematic investigation of these coupled parameters within a combined framework, specifically targeting the early-stage melting dynamics a critical period where the transition from conduction to convection-dominated heat transfer occurs. Unlike previous studies that examined individual parameters in isolation, this work provides the first comparative analysis of rectangular, trapezoidal, and heptahedral enclosures with identical V-shaped fins. The quantifying the joined influence of inclination angle (30°–90°) and heat flux (500–2000 W/m^2) on the melting performance of five commercially relevant PCMs. Furthermore, this study establishes practical selection criteria for PCM and fin materials personalized to specific thermal management applications, based on the trade-off between melting rate and temperature uniformity. This work analyzes the effect of using different inclination angles, from 30° to 90°, with RT-27 as the PCM. The analysis focuses on temperature profiles, the way the liquid–solid interface changes over time, and the impact of various heat fluxes. The improved heptahedral design is then compared with trapezoidal and rectangular configurations in terms of heat transfer coefficients. The simulation results are utilized to establish a relationship connecting the Fourier number with the Nusselt number. Furthermore, this work integrates machine learning prediction models with simulations to accelerate computation. Specifically, Random Forests combined with SHAP analysis are employed for regression analysis. This hybrid method reduces processing time, while the most accurate model is ultimately used to predict the Nusselt number under various heat flux conditions.

Comparison of PCM melting performance with previous studies

For a comprehensive comparison against existing literature, Table 5 summarizes previous numerical studies focusing on PCM melting enhancement. The comparison considers PCM type, enclosure geometry, operating conditions, and key thermal performance metrics, while highlighting the improvements and novel contributions of the present study.

Computational methodology

Physical model

Three different cavity shapes rectangular, trapezoidal, and heptahedral with V-shaped fins are analyzed for liquid fraction, as shown in Fig. 1. Four identical, uniformly distributed, vertical V-shaped fins made of the same material are attached to the right surface of each cavity. The bottom, left, and top surfaces were insulated, while a constant heat flux (Q) is applied to the right surface. Several phase change materials (PCMs) are considered, specifically RT-25, RT-27, RT-31, RT-35, and RT-38. The thermophysical characteristics of these materials are presented in Table 2. Copper, aluminium, and steel are selected as fin materials, and their thermophysical properties are listed in Table 3.

Mathematical model

Numerical model development depend on several key assumptions [12,26,27] .

- The properties of Thermophysics of the PCM and fin materials remain constant.

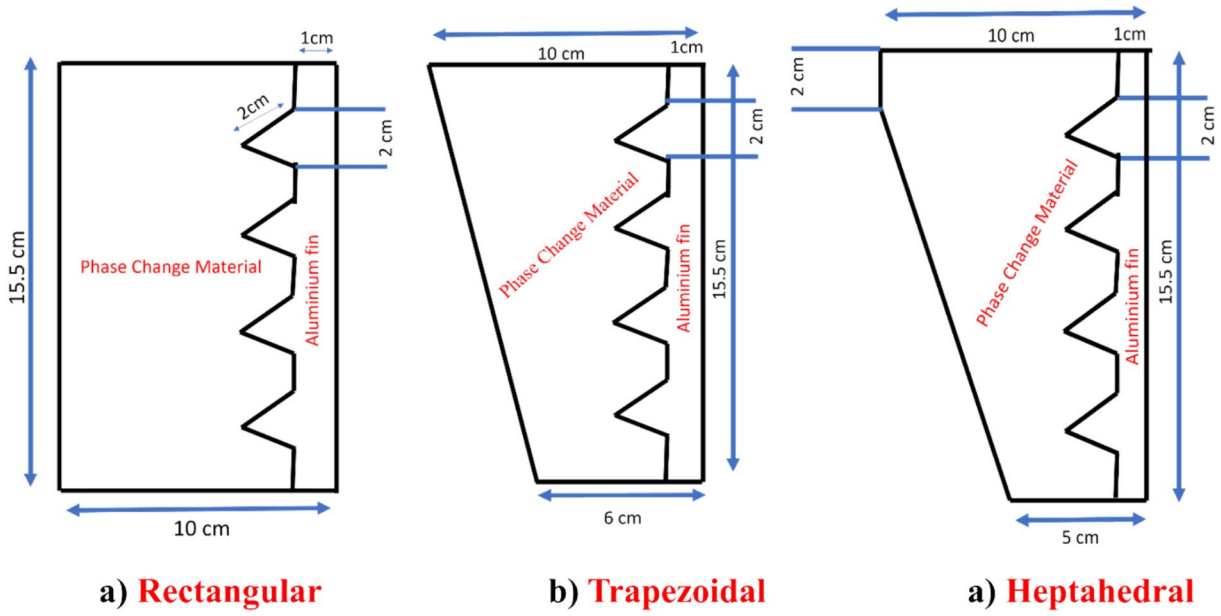


Fig. 1. A schematic illustration of the case (**a**) rectangular (**b**) trapezoidal and (**c**) heptahedral enclosure with "V" shaped fin

- The movement of liquid PCM is considered a two-dimensional, unsteady, laminar, Newtonian, and incompressible flow.
- The change in volume of the phase change material is neglected.
- Heat flux remained constant across the heating surface.
- The density variation of liquid PCM is estimated using the Boussinesq approximation.
- Volume change during melting or freezing is negligible.

Melting and heat transfer in this study are governed by the following equation [26]:

Continuity equation.

$$\frac{\partial \rho}{\partial t} + \nabla .\left(\rho \overrightarrow{v}\right) = 0 \tag{1}$$

Momentum equation

$$\frac{\partial}{\partial t}\left(\rho \overrightarrow{v}\right) + \overrightarrow{v}.\nabla \left(\rho \overrightarrow{v}\right) = -\nabla p + \mu \nabla^2 \overrightarrow{v} + \rho \beta \overrightarrow{g}\left(T - T_m\right) + \overrightarrow{S} \tag{2}$$

Energy equation

$$\frac{\partial}{\partial t}\left(\rho H\right) + \nabla .\left(\rho \overrightarrow{v} H\right) = \nabla .\left(k \nabla T\right) \tag{3}$$

where t is the time, ρ is the density, $\overrightarrow{v}$ is the velocity vector, p is the pressure, μ is the dynamic viscosity, β is the thermal expansion coefficient, $\overrightarrow{g}$ is the gravitational acceleration, T_m is the melting temperature, and k is the thermal conductivity.

Equation (4) is used to determine the source term $\overrightarrow{S}$

$$\vec{S} = A_{mush}\frac{\left(1-\gamma\right)^2}{\gamma^3 + \varepsilon}\vec{v} \tag{4}$$

where A_{mush} is the mushy zone constant, γ is the liquid fraction and ε is a small quantity (=0.001).

Total enthalpy (H) in Eq. (3) is calculated using Eq. (5) [11].

$$\mathrm{H} = \mathrm{h} + \Delta H \tag{5}$$

$$\mathrm{h} = h_{ref} + \int_{T_{ref}}^{T} C_p \Delta T \tag{6}$$

$$\Delta H = \gamma L \tag{7}$$

In Eq. (5–7), h and ΔH respectively sensible enthalpy and latent heat change. h_{ref} corresponds to sensible enthalpy at a reference temperature T_{ref}. L is latent heat of PCM.

The liquid fraction γ can be calculated using equation

$$\gamma = \begin{cases} 0 if T < T_s\left(solid phase\right) \\ \frac{T-T_s}{T_l-T_s} if T_s < T < T_l\left(phase change\right) \\ 1 if T > T_l\left(liquid phase\right) \end{cases} \tag{8}$$

Numerical methodology

The governing equations are solved using ANSYS Fluent based on the finite volume method (FVM). A pressure-based transient solver with the SIMPLE algorithm is employed for pressure velocity coupling. The momentum and energy equations are discretized using the second-order upwind scheme, while the PRESTO scheme and the least squares cell-based method are adopted for pressure interpolation and gradient evaluation. A uniform heat flux of 500 to 2000 W/m^2 is applied to the right wall, while the remaining walls are assumed adiabatic with no-slip boundary conditions. The V-shaped fins are thermally coupled with the PCM by enforcing continuity of temperature and heat flux at the fin PCM interface. Initially, the entire domain is maintained at 297.15 K, below the melting temperature of the PCMs with zero initial velocity. The thermophysical properties of the PCMs and fin materials are listed in Tables 1 and 2. The simulations assumed laminar, incompressible flow with the Boussinesq approximation for buoyancy effects. The melting process is simulated using the enthalpy-based method. The mushy zone is modeled with the liquid fraction determined from the solidus and liquidus temperatures. A mushy zone constant of 10^5 kg m^{-3} s^{-1} is adopted after a compassion analysis which showed deviations in liquid fraction of less than 0.5%. Residual convergence criteria of 10^{-6} for the energy equation and 10^{-4} for the continuity and momentum equations are specified. A time step of 0.1 s determined from the time-step independence study, is used throughout the transient simulations. Under-relaxation factors of 0.3 (pressure), 0.7 (momentum), and 0.9 (energy) are employed to ensure stable convergence (Table 3).

Independency analysis

A grid independence test is carried out to establish the optimal mesh that ensures result accuracy while maintaining computational efficiency. The study is conducted on a rectangular enclosure with an aluminium fin,

References	PCM/geometry	Enhancement method	Comparison with present study
Li et al. (2023)[28]	RT-25/rectangular	Rectangular and parallelogram fins	The heptahedral enclosure reduced melting time by 20.4% and increased the liquid fraction by 34.9% compared with the rectangular enclosure
Tabassum et al. (2017)[29]	Paraffin wax/triangular annulus	Inner-tube geometry optimization	The present study introduces a heptahedral enclosure, demonstrating enhanced melting through enclosure optimization
Ji et al. (2018)[30]	RT-42/rectangular	Double horizontal fins	The present study improves melting performance by optimizing enclosure geometry rather than fin dimensions
Qin et al. (2021)[31]	Lauric acid/rectangular	Bilateral HTF flow	The present study combines heptahedral geometry, V-shaped fins, Random Forest and SHAP model ($R^2 = 0.9729$)
Present study	RT-27/rectangular, trapezoidal, heptahedral	Geometry optimization + V-shaped fins + RF–SHAP analysis	

Table 1. Comparison of the present study with previous investigations on PCM melting enhancement.

PCM	RT-25	RT-27	RT-31	RT-35	RT-38
Density, ρ (kg/m^3)	770	870	760	770	780
Specific heat, C_p (kJ/kgK)	2000	2400	2000	2000	2000
Thermal conductivity, k (W/mK)	0.2	0.24	0.2	0.2	0.2
Dynamic viscosity, μ (kg/ms)	0.02	0.00342	0.02	0.02	0.02
Latent heat of fusion, L_h (kJ/kg)	160	179	165	160	170
Solidus temperature, T_s (°C)	21	24	29	32	34
Liquids temperature, T_l (°C)	25	29	34	38	39

Table 2. Physical properties of different PCM [26].

Fin	Aluminium	Copper	Steel
Density,ρ (kg/m^3)	2719	8978	8030
Specific heat, C_p (kJ/kgK)	871	381	502.48
Thermal conductivity, k (W/mK)	202.4	387.6	16.27

Table 3. Physical properties of different fin.

using three meshes consisting of 17,935, 28,330, and 37,431 quad cells. The test analyzed the temporal variations in liquid fraction (LF) and average temperature (T_{avg}) across the different grids.

Figure 2 presents these variations for the three mesh sizes. Grid 3 is chosen as the best option because it provides an ideal balance between saving computing power and maintaining numerical precision for the later simulations. The numerical meshes are designed to meet quality criteria, with an aspect ratio below 12 and orthogonal quality above 0.56. The skewness values ranged from 3.436×10^{-2} (minimum) to 0.7873 (maximum). Figure 3 illustrates a representative mesh structure for the three model geometries.

Discretization uncertainty analysis

To further verify the reliability of the numerical simulation, a discretization uncertainty analysis is carried out using the grid convergence index (GCI) method. Unlike the grid independence study which only examines the stability of the results GCI method provides a quantitative estimate of the numerical uncertainty caused by spatial discretization. Three successively refined meshes are considered for the rectangular enclosure (Case 1) with RT-27 PCM, aluminium fins, $\alpha = 0°$, and a heat flux of 1000 W/m^2. The meshes consisted of 17,935, 28,330, and 37,431 elements, representing the coarse, medium, and fine grids. The corresponding liquid fraction values at t = 1500 s are listed in Table 4.

The grid refinement factors between the successive meshes are $r_{21} = 1.62$ and $r_{32} = 1.58$, giving an average refinement factor of approximately 1.60. Using Richardson extrapolation, the observed order of convergence is found to be p = 2.37, which is close to the expected second order accuracy of the numerical scheme. The Grid Convergence Index for the fine grid solution is computed as [32]:

$$GCI_{fine} = \frac{F_S \left| \frac{\phi_2 - \phi_1}{\phi_1} \right|}{r_{21}^p - 1} \times 100\% = 1.74\% \tag{9}$$

The GCI for the fine grid solution is calculated as 1.74%, indicating that the uncertainty associated with spatial discretization is less than 2%. Since this value is close to unity, the three meshes can be considered to lie within the asymptotic range of convergence. These results confirm that the numerical uncertainty remains below 2% for all three enclosure geometries.

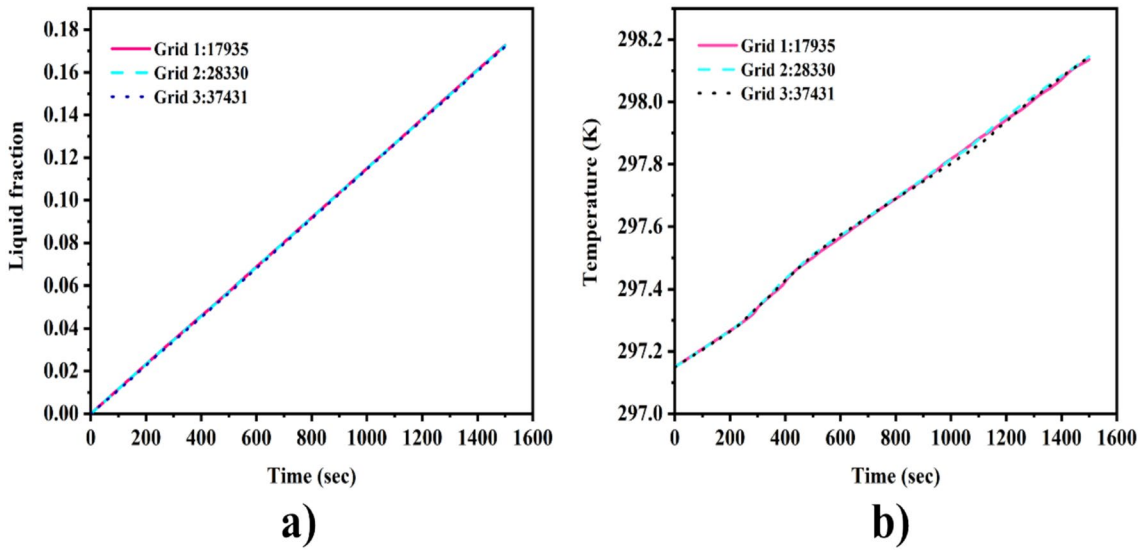


Fig. 2. Variations of (**a**) liquid fraction and (**b**) temperature with time for different grids

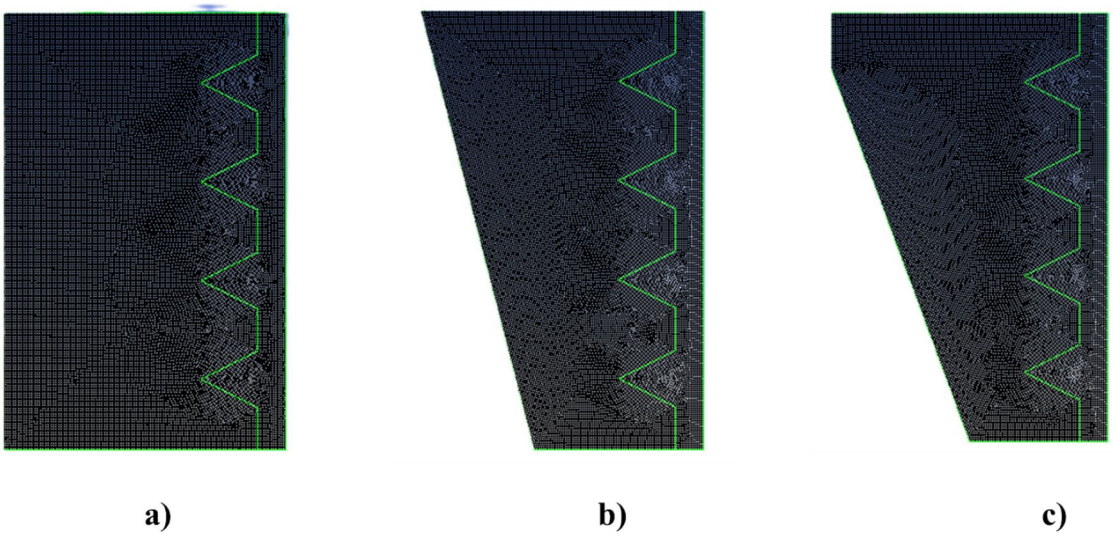


Fig. 3. Computational meshes for (**a**) case 1, (**b**) case 2 and (**c**) case 3.

Grid	Number of elements	Representative cell size (h)	Liquid fraction (LF)	Relative deviation (%)
Coarse (G1)	17,935	h_1	0.168	2.89
Medium (G2)	28,330	h_2	0.172	0.58
Fine (G3)	37,431	h_3	0.173	base

Table 4. Grid independence and discretization uncertainty analysis for the rectangular enclosure (Case 1) at $t = 1500$ s.

Model validation

To verify the accuracy of the current computational method, a validation study is conducted using the published work of L.G. Silva Junior et al. [27]. The validation geometry consists of a two-dimensional rectangular cavity with a height of 0.15 m and a width of 0.10 m, filled with lauric acid as the PCM and equipped with an aluminum fin. All cavity walls are adiabatic except the right wall, which is subjected to a time-dependent heat flux. Figure 4 compares the liquid fraction (β) contours obtained in the present study with those reported by Silva Junior et

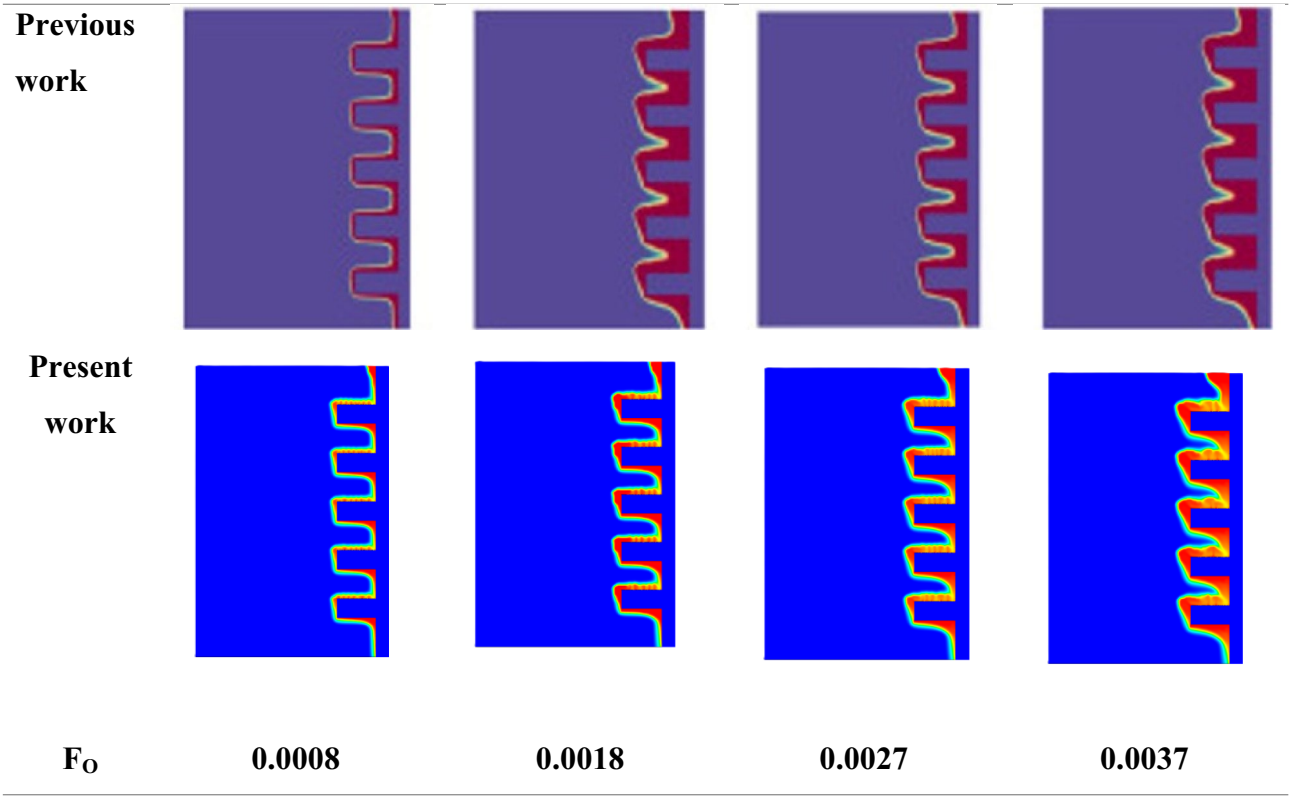


Fig. 4. Numerical analysis of liquid fraction contours for different Fourier numbers is validated [27]

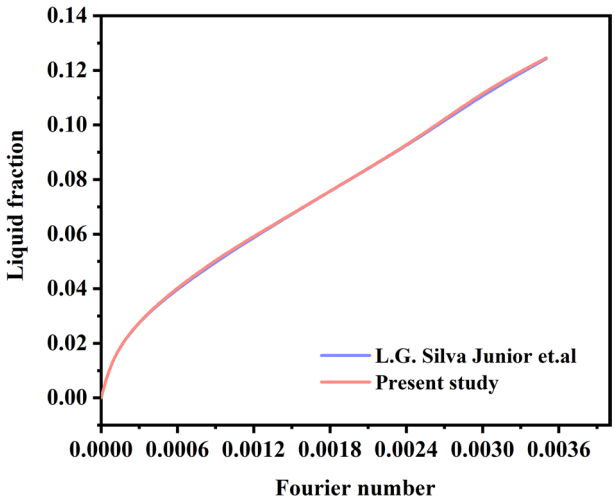


Fig. 5. Comparison of liquid fraction with Fourier number for the present study and L.G. Silva Junior et.al [27]

al. [27] at Fourier numbers of 0.0008, 0.0018, 0.0027, and 0.0037 during the melting process. The comparison demonstrates excellent qualitative agreement between the two sets of results throughout the melting period.

To further quantify the accuracy of the numerical model, a quantitative error analysis is performed by comparing the predicted liquid fraction with the reference data at the selected Fourier numbers. The maximum relative error is found to be 2.83% at Fo = 0.0037, while the average relative deviation is only 1.62%. In addition, the root mean square error (RMSE) of the liquid fraction predictions is calculated as 0.0187. These low error values indicate excellent agreement between the present numerical results and the published reference data, thereby confirming the accuracy and reliability of the computational model. Figure 5 compares the transient liquid fraction (β) variation with Fourier number (Fo). It obtained from the present numerical simulation and the reference study [27] for Case 1 with five fins of 2 cm length. The close agreement observed in both the contour

distributions (Fig. 4) and the liquid fraction (Fig. 5), together with the quantitative error analysis. The present numerical model is validated demonstrating its suitability for following parametric investigations.

Result and discussion

This section presents the results from a series of numerical simulations. The several commercially available PCMs (RT-25, RT-27, RT-31, RT-35, and RT-38) along with different fin materials (aluminium, copper, and steel), all placed inside a rectangular enclosure that includes a V-shaped fin. The effects of inclination angle (30°, 50°, 70°, and 90°), heat flux (500, 1000, 1500, and 2000 W/m^2), heat transfer coefficient, and Nusselt number are evaluated. Together, the parameter ranges and the detailed heat transfer and Nusselt number analysis produce new data and correlations, which support the development of better predictive models for thermal systems using PCMs. Comparison with previously published works highlights the significance and originality of the results. Finally, Random Forest (RF) and SHapley Additive exPlanations (SHAP) analyses are applied to predict the Nusselt number under varying heat flux conditions.

The effect of various PCM and fin materials

Figure 6 shows a) the liquid fraction and b) the temperature over time for different PCM at $\alpha = 0°$ and $Q = 1000$ W/m^2 in a rectangular enclosure (case 1). The liquid fraction (LF, Fig. 6a) represents the proportion of PCM that has melted. Initially, all PCMs are in the solid state, with a liquid fraction of zero. Over time, as the PCMs absorb heat and transition from solid to liquid, the liquid fraction increases. Several key observations can be made: RT-27 demonstrates the slowest melting rate. After 1500 s, it reaches a liquid fraction of only 0.1721, indicating a more gradual transition to the liquid state compared to the other PCMs. RT-25 and RT-38 exhibit the fastest melting rates, both fully melting in approximately 1500 s. RT-35 also melts relatively quickly but not as rapidly as RT-25 and RT-38, achieving a liquid fraction of 0.2115 by 1500 s. These results highlight a few key thermal properties worth noting. The phase transition duration and the thermal response rate. Both play a critical role in applications like temperature control, energy storage, and thermal management. Based on these findings, specific PCMs can be recommended for particular applications. When it comes to thermal energy storage, solar heating, and passive cooling, the best PCMs are those that work over a wide temperature range, take a longer time to change phase, and store a large amount of latent heat. Therefore, RT-27 and RT-25 are appropriate choices for these purposes, with RT-27 being the recommended option.

A measured initial temperature (Fig. 6b) is implemented for all profiles to isolate the effects of each PCM's property. Since the initial conditions are uniform any observed differences in the temperature profiles can be traced back to the PCMs themselves. The following observations are made: RT-27 demonstrates the lowest temperature rise, reaching 295.68 K after 1500 s. This indicates that RT-27 absorbs heat more slowly than the other phase change materials (PCMs). RT-25 shows a moderate temperature increase. It reaching about 305.66 K after 1500 s. Its performance is somewhat superior to that of RT-27, suggesting greater heat absorption efficiency. RT-35 shows a clearer temperature rise, reaching roughly 308.75 K, which points to much stronger heat absorption than RT-25, RT-27, and RT-31. RT-38 follows a similar pattern to RT-35, only with a slightly higher final temperature good, but not the best compared to the other PCMs. The results clearly show that different PCMs exhibit distinct thermal behaviours under identical conditions. These temperature variations reflect differences in heat absorption and storage capacities, which are likely due to the unique thermal characteristics of each PCM.

Figure 7 presents the transient (a) liquid fraction and (b) temperature for different fin materials (aluminium, copper, and steel) at RT-27, an angle of inclination (α) of 0°, and a heat flux (Q) of 1000 W/m^2 in the rectangular enclosure (Case 1). The melting rate of the LF and the average temperature depend on the fin material. Steel exhibits a slower melting rate compared to aluminium and copper, which is expected since the thermal

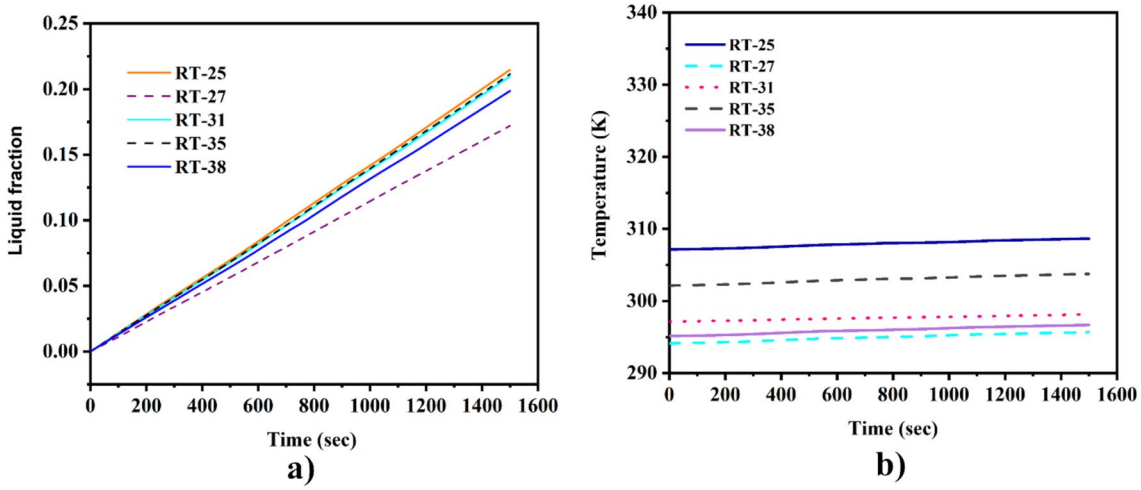


Fig. 6. (**a**) Variation of liquid fraction and (**b**) temperature with time for different PCM types.

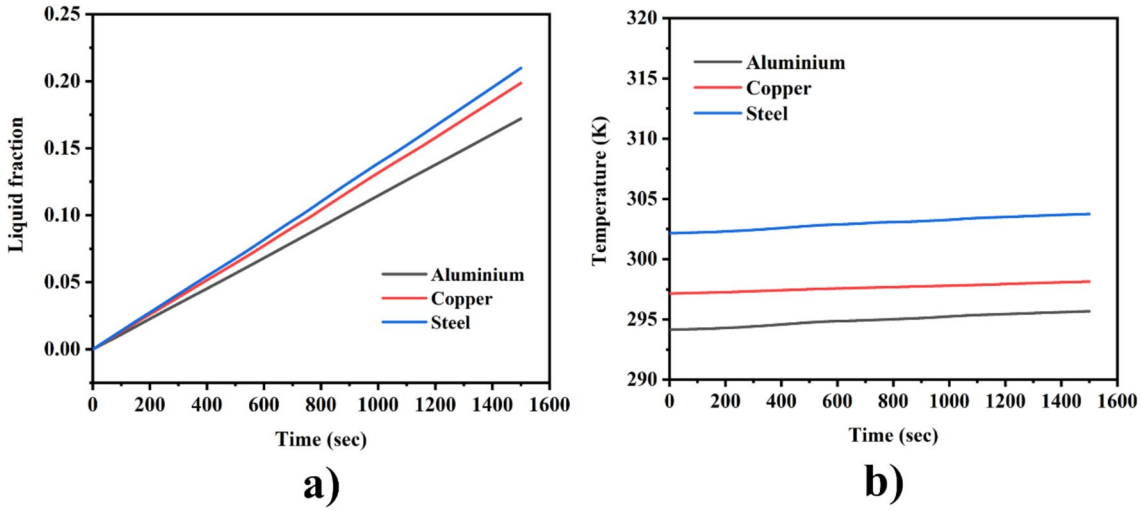


Fig. 7. Changes in (**a**) the liquid fraction and (**b**) the temperature over time for different fin material

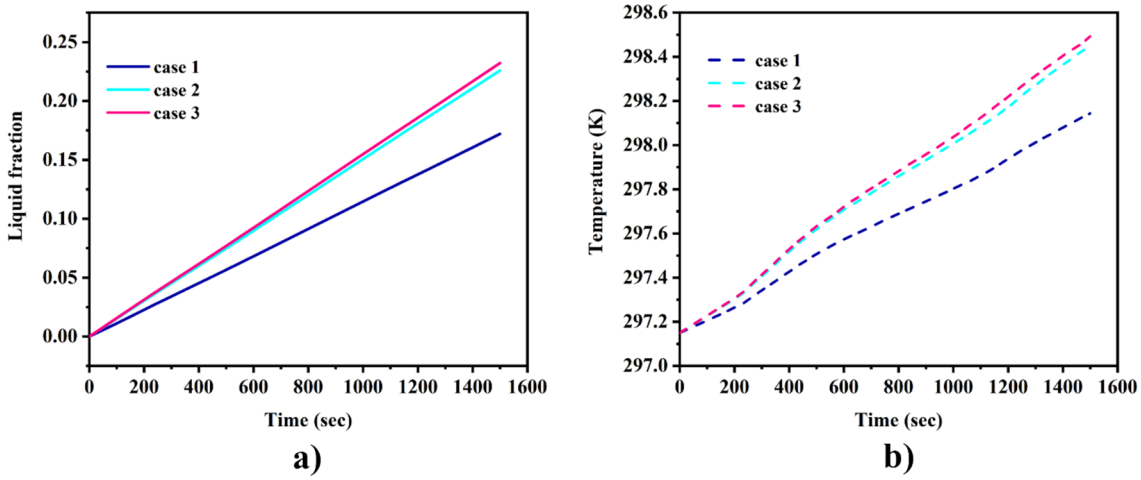


Fig. 8. Numerical analysis of (**a**) liquid fraction and (**b**) temperature with time steps for different cases

conductivity of steel is lower than that of aluminium and copper. Therefore, aluminium and copper are more suitable for these applications, with aluminium being the most favourable choice.

Physically, this behaviour reflects the direct role of fin thermal conductivity in developing the thermal boundary layer adjacent to the heated wall. A highly conductive fin (aluminium, copper) rapidly diffuses heat into the surrounding PCM, thinning the conduction-dominated boundary layer and triggering earlier buoyancy-driven natural convection. However, the lower conductivity of steel keeps conduction the dominant passage mechanism for longer, suspending the onset of convective circulation and the associated increase in melting rate.

Comparison of melting characteristics for different cases

Figure 8 shows (a) the liquid fraction and (b) the temperature distribution for various structures (rectangular, trapezoidal, and heptagonal). The fin material is aluminium, the PCM is RT-27, and $Q = 1000\ W/m^2$, at different times. Figure 8a illustrates the variation of the LF over time during PCM melting for the three cases. Initially, the liquid fraction is nearly the same for all three structures, but it progressively increases as melting proceeds. The trapezoidal (case 2) and heptagonal (case 3) structures melt more quickly than the rectangular (case 1) structure, with case 3 exhibiting the fastest melting rate. At 1500 s, the liquid fractions for cases 2 and 3 are 0.225 and 0.232, respectively, confirming their superior melting performance.

Figure 8b shows the temperature changes over time (in seconds) for different cases. The temperature trends are very similar across all three cases. In Case 1, the average temperature rises considerably faster, while Cases 2 and 3 delay behind Case 1 by approximately 130 s in terms of temperature increase. Once melting is complete, the temperature in Cases 2 and 3 is slightly greater than in Case 1. Furthermore, the average temperature in Case 3 is higher than in Case 2. As melting progresses, the contact area between the solid and liquid decreases, leading to slower melting but a faster rate of temperature rise.

Figure 9 displays the contours of the liquid fraction for RT-27 at a heat flux of 1000 W/m^2 for various enclosure shapes over time. At 500 s, the PCM has only melted partially. The boundary between solid and liquid stays parallel to the heated wall on the right, which means heat conduction is still the main player at this stage. By 1000 s, the liquid PCM at the top of the rectangular (Case 1) enclosure reaches the right wall. However, the trapezoidal (Case 2) and heptagonal (Case 3) enclosures contain a larger quantity of liquid PCM near the top, which promotes stronger convective heat transfer. As a result, the liquid phase has not yet reached the left wall in these cases. It is also evident that as time increases, the PCM melts more significantly near the right wall in all cases, accelerating the overall melting process.

The parallel solid–liquid interface observed at 500 s corresponds to a conduction-dominated regime, in which heat transfer is governed purely by diffusion through the thin layer of molten PCM adjacent to the heated wall. As the liquid layer thickens, the growing temperature difference across it destabilizes the melt through buoyancy. Its natural convection cells that passage hot liquid PCM toward the top of the enclosure. This conduction-to-convection transition clarifies the trapezoidal and heptahedral enclosures. It provide more space for the convection cell to develop accumulate liquid PCM near the top more rapidly than the rectangular enclosure.

Quantitative performance comparison of enclosure geometries

A quantitative comparison of the three enclosure geometries is presented in Table 5, summarizing the key performance indicators at (t = 1500 s) under identical operating conditions (RT-27 PCM, aluminum fins, α = 0°, Q = 1000 W/m^2). The heptahedral enclosure (Case 3) exhibits the best thermal performance achieving a liquid fraction of 0.232. It is 34.9% higher than the rectangular enclosure (Case 1) and 3.1% higher than the trapezoidal enclosure (Case 2). The melting completion time is reduced from 1520 s in Case 1 to 1210 s in Case 3 corresponding to a 20.4% reduction, while a 4% reduction is observed compared with Case 2. These results indicate that the heptahedral geometry significantly accelerates the melting process and enhances the thermal

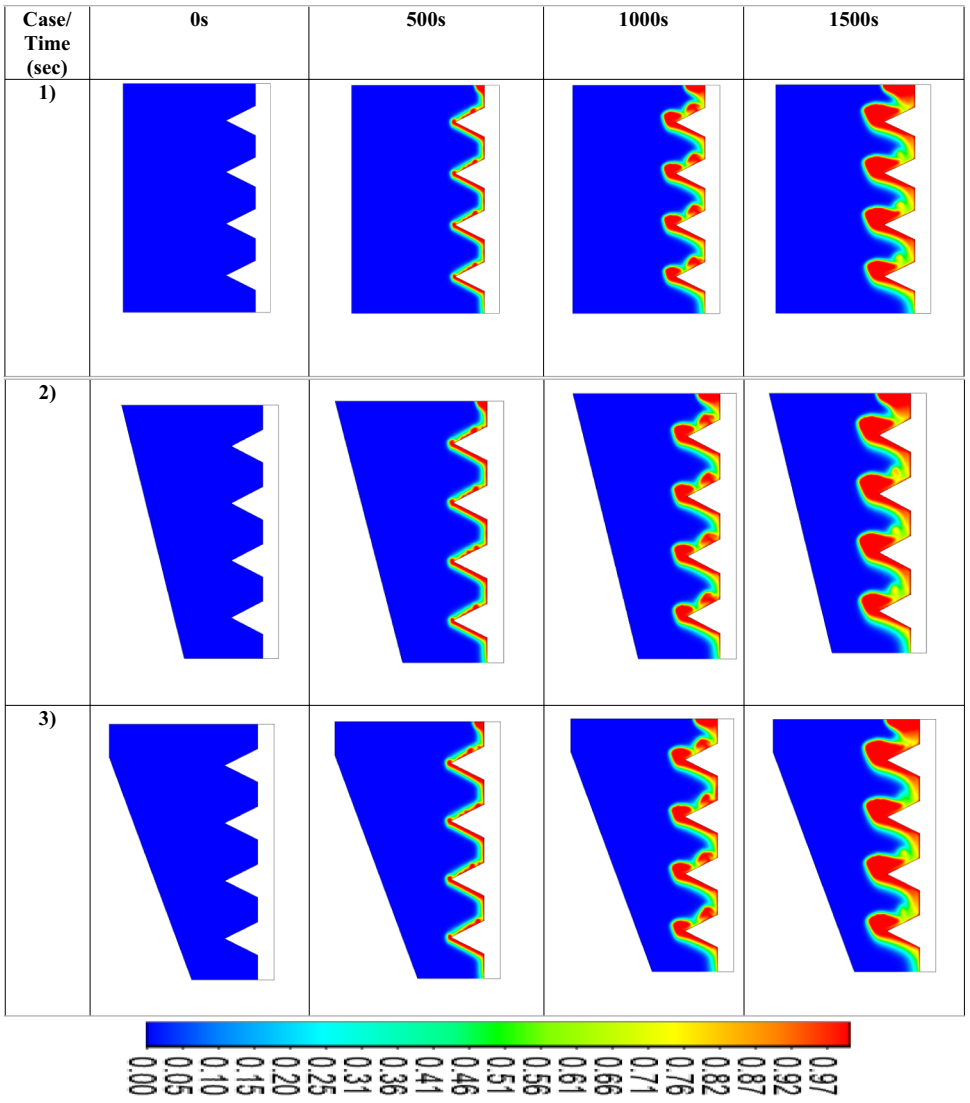


Fig. 9. Liquid fraction profiles are shown for (**a**) Case 1, (**b**) Case 2, and (**c**) Case 3 at various time intervals (s)

Performance metric	Case 1	Case 2	Case 3	Improvement (Case 3 vs. Case 1)	Improvement (Case 3 vs. Case 2)
Liquid fraction (LF)	0.172	0.225	0.232	34.9%	3.1%
Average temperature (K)	297.48	298.13	298.49	0.34%	0.12%
Maximum temperature (K)	298.02	298.67	299.14	0.38%	0.16%
Melting completion time (s)	1520	1260	1210	20.4%	4.0%
Temperature uniformity	0.54	0.54	0.65	–	–

Table 5 . Quantitative comparison of thermal performance for different enclosure geometries at t = 1500 s.

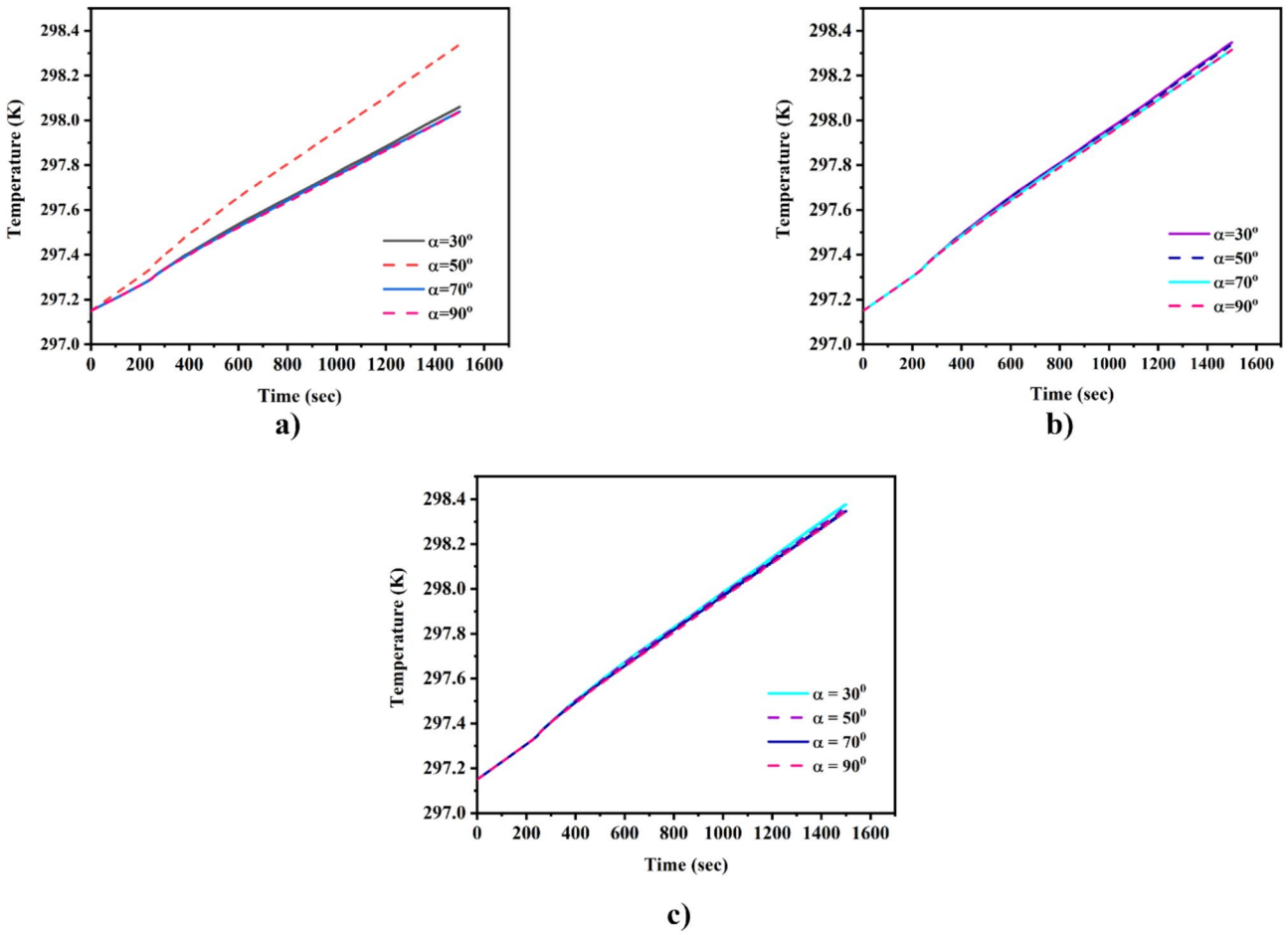


Fig. 10. Temperature variation with time (sec) for (**a**) case 1, (**b**) case 2 and (**c**) case 3 at different angles (α)

charging performance. The average and maximum temperatures in the heptahedral enclosure reach 298.49 K and 299.14 K which are slightly higher than those of the other two geometries. Although the temperature differences are relatively small, they indicate improved heat absorption and more effective melting. The superior performance of the heptahedral enclosure is primarily attributed to its geometric configuration. They promote stronger natural convection and improve melted PCM circulation within the cavity. Overall, the quantitative results presented in Table 5 clearly demonstrate that the heptahedral enclosure provides the most effective thermal performance among the three geometries, making it a promising design for latent heat thermal energy storage applications.

The effect of cavity angle for different cases

Figure 10 illustrates the variation of inclination angles for temperature over time at R = 27 and Q = 1000 W/m^2. All temperature profiles begin at a baseline of 297.15 K, demonstrating consistent starting conditions for every case. This uniformity ensures that any differences in the temperature profiles are due to the inclination angle in the initial temperature. However, both the rate and magnitude of temperature change are significantly influenced by α across the various cases.

For α = 30° and 50° These angles exhibit a slight increase in temperature for cases 1, 2, and 3. At the end of the time, the temperature at α = 50° is slightly higher than that at α = 30°, but significantly lower compared to steeper angles. Furthermore, for α = 30°, case 3 shows a greater incline than both case 1 and case 2.
For α = 70° and 90° These angles demonstrate the most rapid temperature increases across all three cases. At α = 70°, the temperature in case 3 approaches approximately 298.34 K, while at α = 90°, it exceeds 298.49 K. This suggests a more efficient heat absorption process at steeper angles, particularly in case 3.

These findings suggest that RT-27 absorbs heat most effectively when positioned closer to vertical in all cases. It clearly demonstrates a strong relationship between temperature distribution and inclination angle across the three cases. The trend indicates that the heat absorption performance of RT-27 is maximized at steeper angles. At 90°, the surface area facing the heat source is more optimally positioned resulting in improved absorption and a larger temperature rise. The inclination angle may also influence convective flows within RT-27, enhancing the rate of heat transfer at sharper angles. Also, the structure and composition of RT-27 may promote greater heat absorption when placed at higher inclinations.

Figure 11 shows the liquid fraction of RT-27 over 1500 s at different angles (α = 30°, 50°, 70°, and 90°) under a constant heat flux (Q = 1000 W/m^2) for three cases. For all angles, the liquid fraction of RT-27 increases over time, demonstrating the solid-to-liquid phase change. The liquid fraction approaches its maximum value, indicating nearly complete melting as time progresses. As the angle α increases from 30° to 90°, the change in the liquid fraction becomes more pronounced, with the curves exhibiting steeper slopes compared to the other cases. This indicates faster melting due to stronger natural convection flows that enhance heat transfer. The differences in the liquid fraction profiles highlight the significant impact of α on the thermal behavior of RT-27. These results suggest that the orientation of the PCM container considerably affects the melting rate because of the varying influence of natural convection and gravity.

The effect of different heat flux for various cases

Figures 12 and 13 illustrate the variation of liquid fraction (LF) over time for RT-27 at an angle (α) of 0° under cases (1, 2, and 3), considering different heat flux (Q) values. Four distinct Q values are examined: 500, 1000, 1500, and 2000 W/m^2. For all Q values, the LF initially rises slowly from 0 to about 0.1 within the first 1000 s, indicating the onset of melting in the RT-27 material. After this stage, the LF increases at a noticeably faster rate, which is directly dependent on the extent of Q. At Q = 500 W/m^2, the LF raises gradually, reaching 0.113, 0.117, and 0.119 at around 1500 s for cases 1, 2, and 3, respectively. It reflecting a slower phase transition compared to higher Q values. At Q = 1000 W/m^2, the LF increases more rapidly, achieving complete melting within 1100 s across all three cases. For higher Q values of 1500 and 2000 W/m^2, the melting process is even faster, with case 3 completing phase change in 650 and 410 s. This demonstrates the accelerated phase transition under higher heat loads. As these results illustration the phase change rate doesn't increase in a simple, linear way with heat flux instead, larger heat flux values give the melting process a significant improvement. Consequently, higher heat fluxes enable rapid phase transition, making RT-27 well-suited for applications requiring fast thermal energy absorption and storage.

Figure 14 illustrates the average temperature variation over time for different heat flux values using three cases at RT-27. The investigation considers four heat flux values: Q = 500, 1000, 1500, and 2000 W/m^2. For each heat flux value, the initial temperature remains stable around 297.15 K at the start of the simulation. This stable period corresponds to a phase in which RT-27 absorbs heat, while its thermal inertia. The phase change characteristics limit the rise in average temperature. At Q = 500 W/m^2, the temperature increases gradually, reaching approximately 297.73 K, 297.59 K, and 297.75 K for the three cases by the end of the time at 1500 s. When Q increases to 1000 W/m^2, the temperature rise becomes more pronounced, reaching 298.14 K, 298.45 K, and 298.49 K for the three cases at 1500 s. The temperature increase is even more significant at higher heat fluxes. At Q = 1500 W/m^2, the temperature rises suddenly, reaching about 299.53 K for case 3. At Q = 2000 W/m^2, the temperature exceeds 301.21 K for case 3 at 1500 s, demonstrating a highly sensitive response to stronger heat flux values.

Dimensionless analysis

The influence of heat transfer coefficient (HTC) and Nusselt number (Nu) on Fourier number (Fo) is analyzed for Case 3 at RT- 27 under varying heat flux conditions (500, 1000, 1500, and 2000 W/m^2). Figures 15 and 16 illustrate the relationship between the Nusselt number (Nu) and the Fourier number (Fo) for multiple strategies. The Fourier number (F_o) is defined as [27]

$$F_o = \frac{t}{t_d} \tag{10}$$

Thermal diffusivity (α) in Eq. (9) is calculated using Eq. (10)

$$t_d = \frac{L^2}{\alpha} \tag{11}$$

$$\alpha = \frac{k}{\rho C_p} \tag{12}$$

where t is a time (in second), L is a characteristic length, k is thermal conductivity, ρ is the density and C_p is the specific heat.

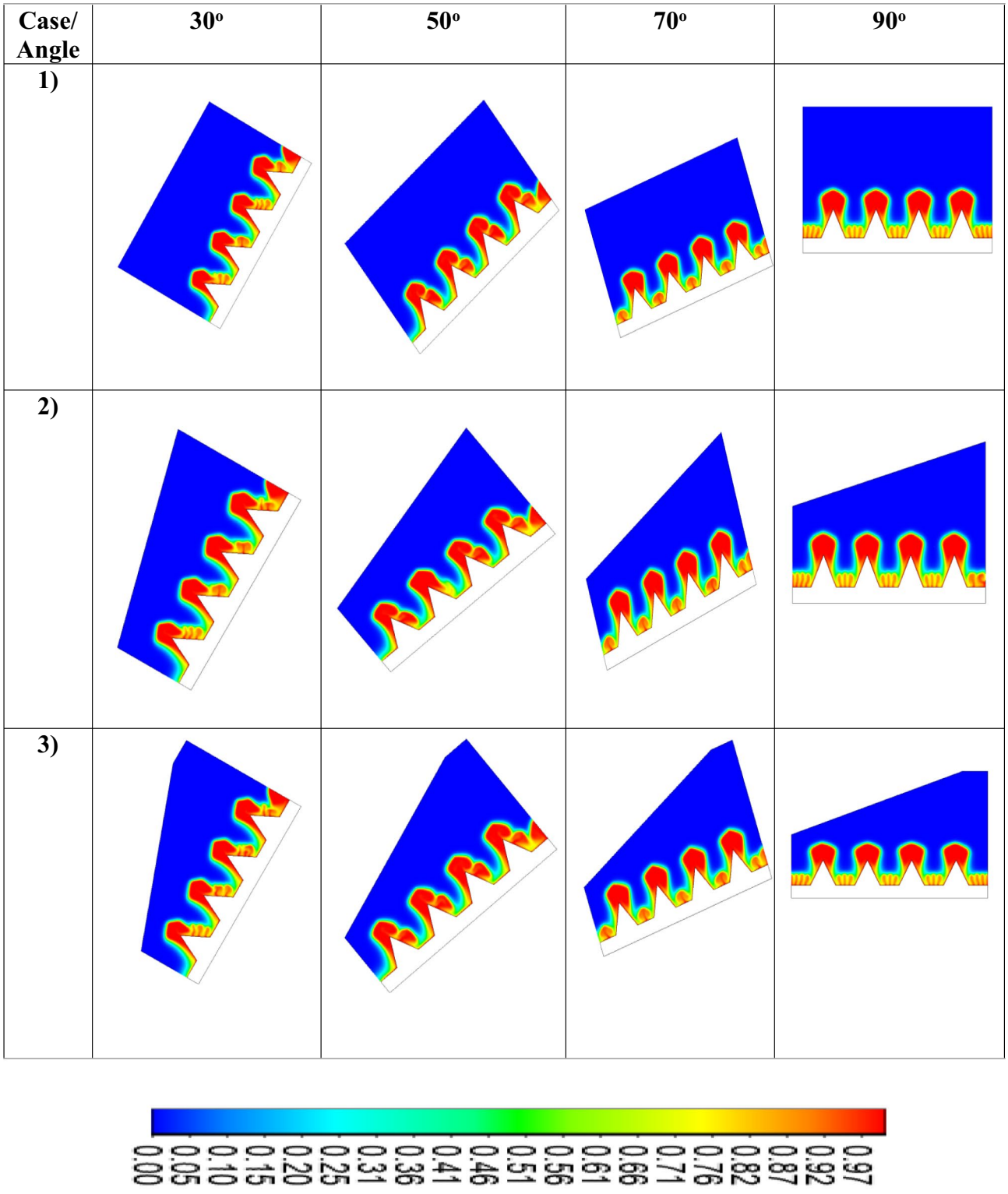


Fig. 11. The contours of liquid fractions for cases 1, 2, and 3 of different angles with time (sec) = 1500 s

Heat transfer coefficient (HTC)

Figure 15 shows the variation of heat transfer coefficient (HTC) of RT-27 changes over time at four different heat flux levels (Q) in case 3. At Q = 500 W/m^2, the HTC rises steadily but more slowly than at higher heat flux values. By F_o = 0.0172, the HTC reaches 33.94 W/m^2. At Q = 1000 W/m^{2}K, the HTC increases much more rapidly, demonstrating better performance than at 500 W/m^2. By the end of simulation, the HTC at this heat flux reaches about 57.74 W/m^{2}K. At Q = 1500 and 2000 W/m^2, the HTC values are the highest. The curve for 1500

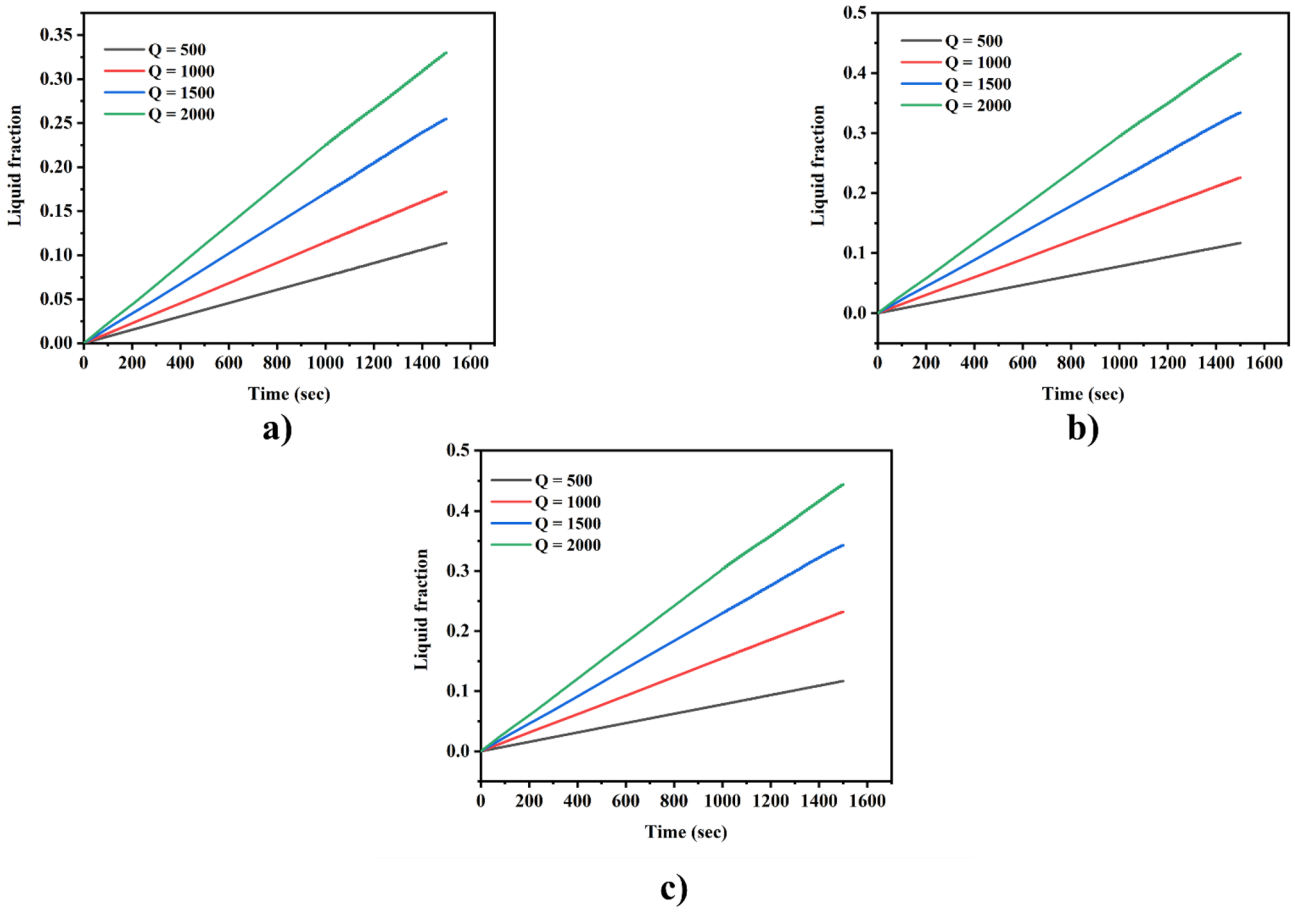


Fig. 12. Liquid fraction variation with time (sec) for (**a**) case 1, (**b**) case 2 and (**c**) case 3 at different heat flux (*Q*

W/m^2 is very similar to that of 2000 W/m^2, though slightly higher, reaching almost 77.56 W/m^{2}K by the end of melting. The 1500 and 2000 W/m^2 heat flux levels show significantly better heat transfer than the lower 500 W/m^2 level. This indicates that increasing the heat flux (Q) enhances RT-27's thermal performance. However, the small difference in HTC between 1500 and 2000 W/m^2 suggests that there are limits to the benefit of further increasing the heat flux. Consequently, the best heat transfer for RT-27 happens when the heat flux is between 1500 and 2000 W/m^2. This is especially accurate for systems that deal with changing conditions and allow you to fine-tune the thermal energy flow for peak performance.

Nusselt number (Nu)

The Nusselt (Nu) number as depicted in Fig. 16 is a key parameter for evaluating the impact of different heat flux levels in case 3. At the initially of the phase change, Nu values pointed due to the steep temperature gradients at the wall, especially when the fin array is near the solid–liquid interface. Interestingly, both Q = 1000 and 1500 W/m^2 exhibited higher overall values compared to Q = 2000 W/m^2, despite the latter initially possessing a greater heat transfer coefficient. These results agree with earlier work. When the heat flux is lower in case 3, convective heat transfer gets stronger, and that results in several distinct boundary layers forming inside the PCM zone. The conclusions highlight significant impact of heat flux variation on the overall Nu, with the Q = 2000 W/m^2 configuration demonstrating superior heat transfer performance. Additionally, the outcomes emphasize crucial role of natural convection compared to conduction in the process of phase change. The flow of convection enhances heat transfer because of the PCM, distributing more effectively using thermal energy than simply conduction. This research reveals that in regions where convection prevails, the rate of heat transfer increases considerably, leading to a more rapid melting process for Q = 2000 W/m^2 in case 3.

The variation of the Nusselt number (Nu) demonstrates the transition from conduction to convection dominated heat transfer during the PCM melting process. At the beginning of melting, Nu reaches a high value because of the large temperature gradient between the heated wall and the solid PCM, where heat transfer occurs mainly by conduction. As melting progresses, the thermal boundary layer develops, causing the Nusselt number to decrease until it reaches a minimum value. This circumstance marks the start of natural convection. For a heat flux of 500 W/m^2, the minimum Nu occurs at Fo = 0.008 (700 s), whereas at 2000 W/m^2 it shifts to Fo = 0.003 (260 s), indicating that higher heat flux promotes an earlier transition to convection. Beyond this point, the Nusselt number increases as buoyancy-driven flow becomes stronger and enhances convective heat transfer.

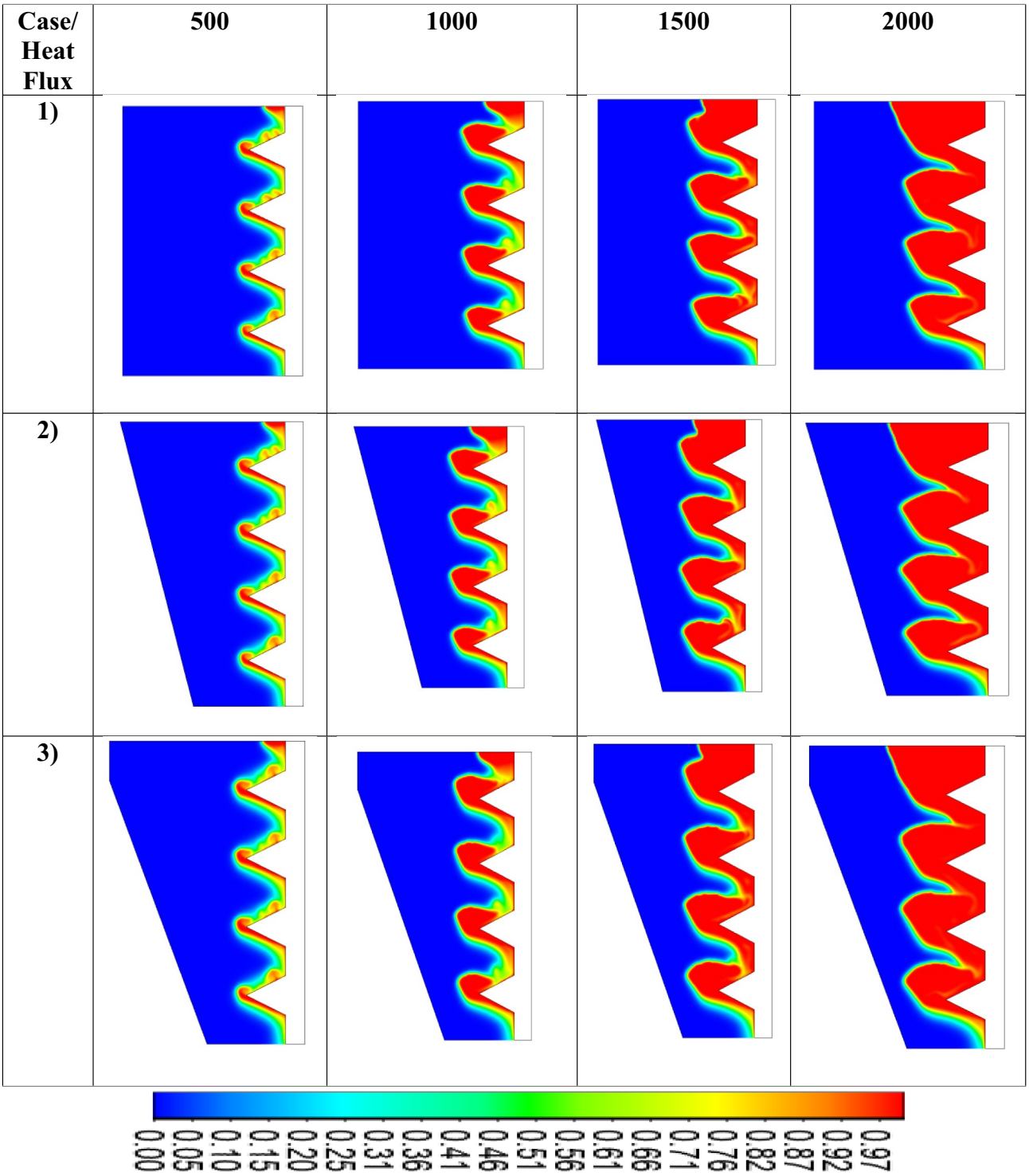


Fig. 13. Liquid fraction contours for (**a**) case 1, (**b**) case 2 and (**c**) case 3 of different heat flux (Q) with time (sec) = 1500 s

At Fo = 0.0172, the final Nu reaches approximately 39 for Q = 2000 W/m^2, compared with about 18 for Q = 500 W/m^2. However, the improvement becomes less significant at higher heat fluxes. The difference in the average heat transfer coefficient between 1500 and 2000 W/m^2 is only about 3%, indicating that natural convection approaches a saturation level, beyond which further increases in heat flux provide only marginal enhancement in thermal performance.

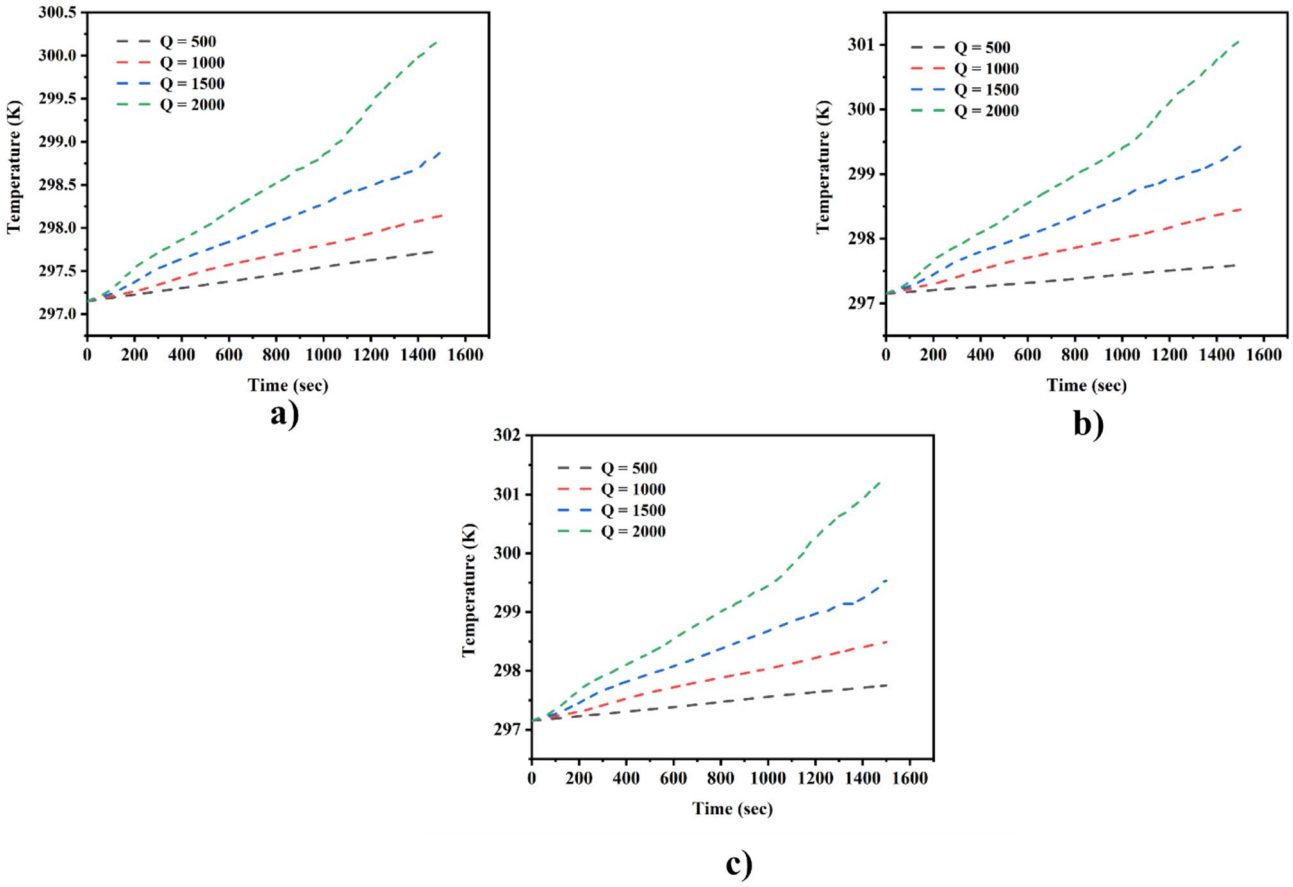


Fig. 14. Temperature variation with time (sec) for (**a**) case 1, (**b**) case 2 and (**c**) case 3 at different heat flux

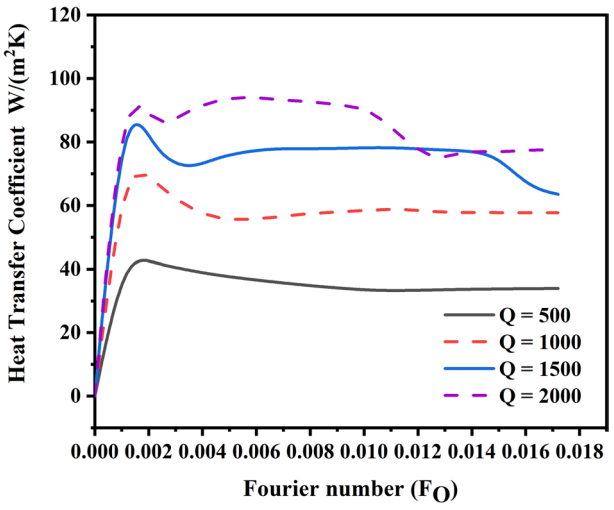


Fig. 15. Heat transfer coefficient as a function of Fourier number

Random forests

Random forest (RF) analysis is a valuable method for determining the importance of input variables. It works by averaging the forecasting of several decision trees, each developed using a random subset of the data. RF is a popular machine-learning technique due to its ease of use and availability as an open-source implementation within the scikit-learn library. The random forest algorithm builds on the bagging technique. However, it goes a step further by only considering a random subset of features, which adds another layer of unpredictability to each tree. This feature randomness, also known as the "random subspace approach" or feature bagging, produces

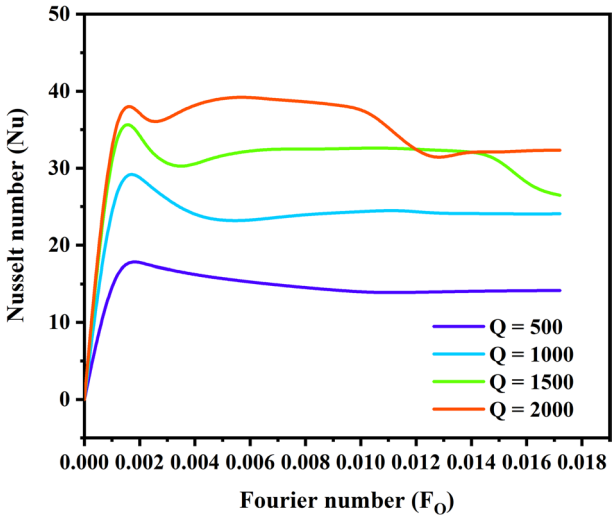


Fig. 16. The relationship between Nusselt number and Fourier number

diverse trees with low correlation, as each tree is trained on a different set of features. As a result, overfitting is reduced and the overall performance of the model is improved.

Random forest (RF) is selected because it provides accurate prediction of nonlinear relationships while maintaining strength against overfitting, even for relatively small CFD-generated datasets. Compared with linear regression and boosting algorithms, RF requires fewer hyperparameter adjustments and offers greater interpretability through feature importance and SHAP analysis. The objective of integrating RF with the present CFD study is not to replace hi-fi simulations but to develop a surrogate model. It capable of rapidly predicting the Nusselt number for new operating conditions after the CFD database has been generated. Similar hybrid numerical machine learning approaches have recently been reported for thermal based management applications, including incompressible thermal hydraulic enhanced by hybrid artificial intelligence, neural-network modelling of magnetohydrodynamic flow with Soret effects, and numerical artificial neural network frameworks for hybrid nanofluid helped enhanced oil recovery [33–36]. These studies demonstrate that join CFD with machine learning provides an efficient approach for accelerating engineering design and optimization while conserving prediction accuracy.

Figure 17 illustrates the random forest algorithm. In our study, the random forest regressor was trained using a dataset split of 80% for training and 20% for testing. The model is developed using the bagging method and evaluated with several error metrics. If the out-of-bag data indicated insufficient predictive accuracy, the RF model was optimized and its accuracy reassessed. Once the model achieved acceptable predictive error during validation, it is applied to the test set for final evaluation.

Once the RF model is trained using the CFD generated dataset, predictions of the Nusselt number for parameter combinations are obtained almost instantly, eliminating the need to perform additional transient CFD simulations for every design case. Therefore, the proposed CFD RF framework significantly reduces computational effort during parametric analysis and optimization while maintaining high prediction accuracy.

Figure 18 illustrates the R^2 values obtained from different random states. The results indicate that random states 9 and 8 yield the highest prediction accuracy for the training and testing datasets, respectively. Specifically, the R^2 value is 0.9896 for the training dataset at random state 9 and 0.9729 for the testing dataset at random state 8.

Figure 19 compares the actual and predicted Nusselt number (Nu) values for a case 3. These predictions are made using random forests, trained and tested on datasets with different heat flux.

Dataset description and model setup

The dataset used to develop the random forest (RF) regression model is generated from the transient CFD simulations of the heptahedral enclosure (Case 3). A total of 960 samples is obtained by considering four heat flux values (500, 1000, 1500, and 2000 W/m^2), four inclination angles (30°, 50°, 70°, and 90°), and the melting period (0–1500 s). Heat flux (Q), inclination angle (α), and time (t) are used as the input features, while the Nusselt number (Nu) is selected as the target variable. The dataset is randomly divided into training (80%, 768 samples) and testing (20%, 192 samples) subsets using a fixed random state to ensure reproducibility. The RF model is implemented using the scikit-learn library with optimized hyperparameters obtained through grid search and 5-fold cross-validation (n_estimators = 100, max_depth = 10, min_samples_split = 5, min_samples_leaf = 2, and random state = 9), providing a balance between predictive accuracy and model generalization.

Model evaluation criteria and performance metrics

The predictive performance of the RF model is evaluated using five widely adopted statistical metrics: the coefficient of determination (R^2), mean squared error (MSE), mean absolute error (MAE), root mean squared

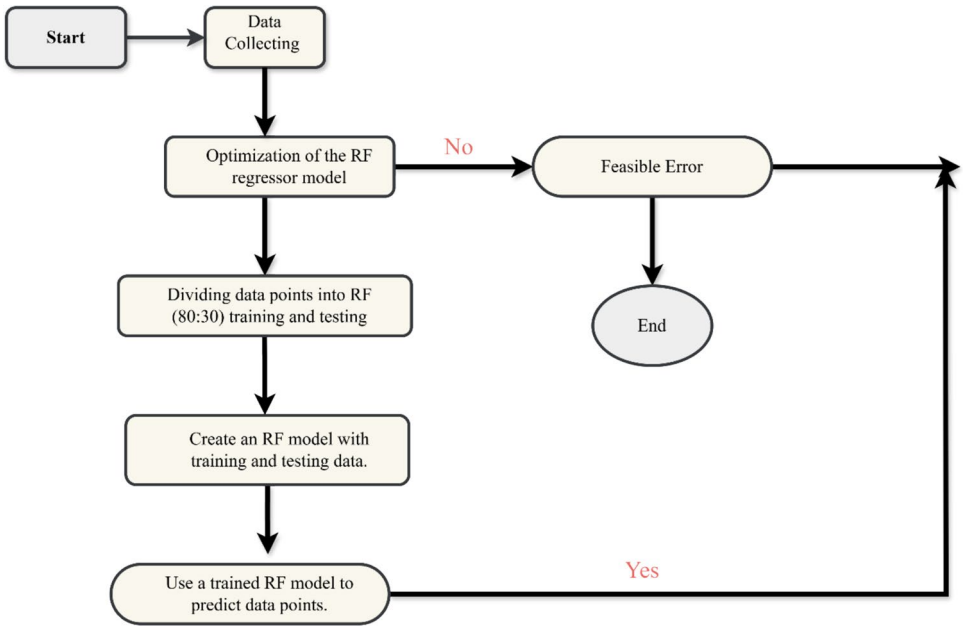
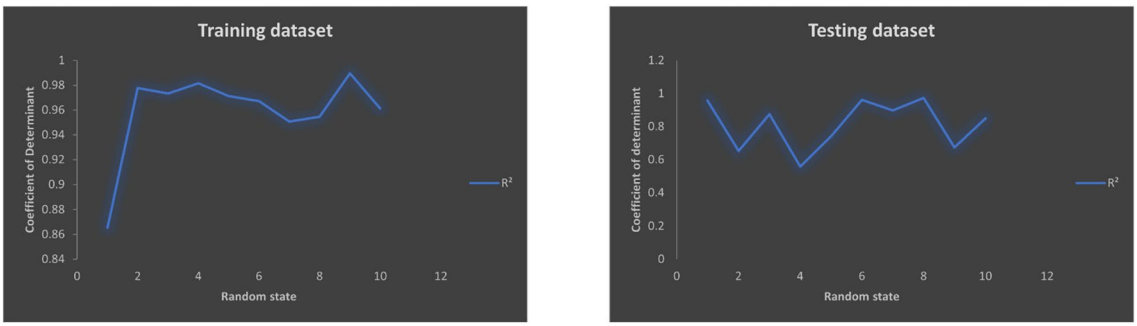


Fig. 17. Random forest (RF) algorithms begin with data collection, which is then split into two sets: a training set (80%) and a testing set (20%).



a) **b)**

Fig. 18. Results of RF showing variation showing variations of R^2 with different random state values for (**a**) training and (**b**) testing datasets

error (RMSE), and mean absolute percentage error (MAPE). Their mathematical formulations are presented in Eqs. (12–16).

$$\mathrm{R2} = 1 - \frac{\sum_{i=1}^{n}(Y_{pred,i} - Y_{real,i})^2}{\sum_{i=1}^{n}(Y_{real,i} - Y_{real})^2} \tag{12}$$

$$MSE = \frac{1}{n}\sum_{i=1}^{n}(Y_{pred,i} - Y_{real,i})^2 \tag{13}$$

$$MAE = \frac{1}{n}\sum_{i=1}^{n} \mid Y_{pred,i} - Y_{real,i} \mid \tag{14}$$

$$RMSE = \sqrt{\frac{1}{n}\sum_{i=1}^{n}(Y_{pred,i} - Y_{real,i})^2} \tag{15}$$

$$\mathrm{MAPE} = \frac{100\%}{n}\sum_{i=1}^{n}\left|\frac{Y_{real,i} - Y_{pred,i}}{Y_{real,i}}\right| \tag{16}$$

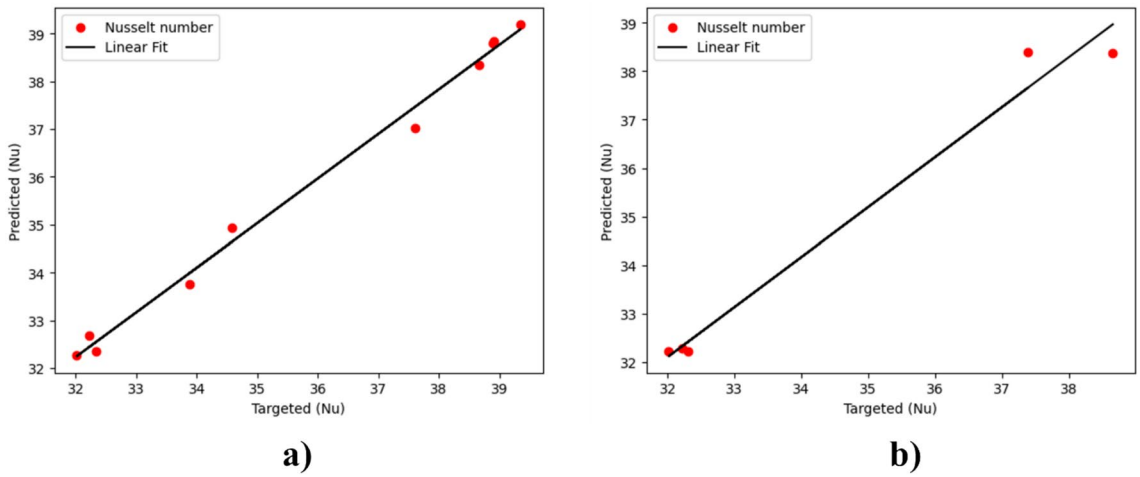


Fig. 19. Validating the RF model by the scatter plot for (**a**) training and (**b**) testing datasets using Nusselt number (Nu)

Dataset	MAE	MSE	RMSE	MAPE (%)	R^2
Training	0.2406	0.0904	0.3007	2.74	0.9896
Testing	0.3218	0.2662	0.4156	3.68	0.9729

Table 6 . Performance evaluation of random forest regression model for Nusselt number prediction.

Table 6 summarizes the performance of the RF model for Nusselt number prediction. The model achieved R^2 values of 0.9896 and 0.9729 for the training and testing datasets, respectively, demonstrating excellent predictive capability. The low testing errors (MAE = 0.3218, RMSE = 0.4156, and MAPE = 3.68%) indicate accurate and reliable predictions with minimal generalization error. The close agreement between the training and testing metrics confirms that the model effectively captures the nonlinear relationship between the operating parameters and the Nusselt number without significant overfitting, highlighting the suitability of the random forest algorithm for surrogate modeling of the CFD-generated dataset.

SHAP analysis

SHAP (SHapley Additive exPlanations) is used to analyze the RF model, examining how each feature variable influences the model's predictions. The x-axis of the SHAP plot represents the SHAP values, which indicate impact of each feature on the target variable's prediction, while the y-axis lists the features. Figure 20 summarizes both global feature importance and local explanations. The global SHAP analysis describes the overall model behavior, whereas the local analysis focuses on individual predictions. Figure 20 shows the significant importance of features each target variable (Q = 500, 1000, 1500, and 2000 W/m^2) using the Nusselt number.

Figure 20a shows that the heat flux levels of Q = 2000 W/m^2 and Q = 500 W/m^2 exhibit the largest mean SHAP values, indicating that these operating conditions contribute most strongly to the Random Forest prediction of the Nusselt number, whereas the intermediate heat fluxes (1000 and 1500 W/m^2) have comparatively smaller contributions. At high heat flux, the larger wall temperature gradient enhances buoyancy-driven natural convection, resulting in faster melting and higher Nusselt numbers. Conversely, at low heat flux, heat transfer remains mostly conduction controlled producing a clearly different thermal response. Consequently, these two operating extremes provide the greatest contrast in heat-transfer behaviour and therefore have the strongest influence on the model predictions. Figure 20b further demonstrates that higher feature values (red points) generally shift the SHAP values toward positive contributions to the predicted Nusselt number, while lower feature values (blue points) contribute negatively. This agreement between the SHAP clarification and CFD observations confirms that the reasonable machine-learning model captures the same fundamental heat transfer rather than acting as a purely numerical predictor. Unlike the CFD simulations, which describe the thermal behaviour of individual operating conditions, the SHAP analysis quantitatively ranks the influence of each input parameter across the entire dataset. Therefore, SHAP provides additional scientific value by identifying the most influential design variables for predicting heat transfer performance, offering useful control for future optimization of PCM enclosure geometry and operating conditions.

Conclusion

This study numerically investigated the early-stage melting behavior of phase change materials (PCMs) in rectangular, trapezoidal, and heptahedral enclosures equipped with identical V-shaped fins. The effects of PCM type, fin material, inclination angle (30°–90°), and heat flux (500–2000 W/m^2) on melting performance

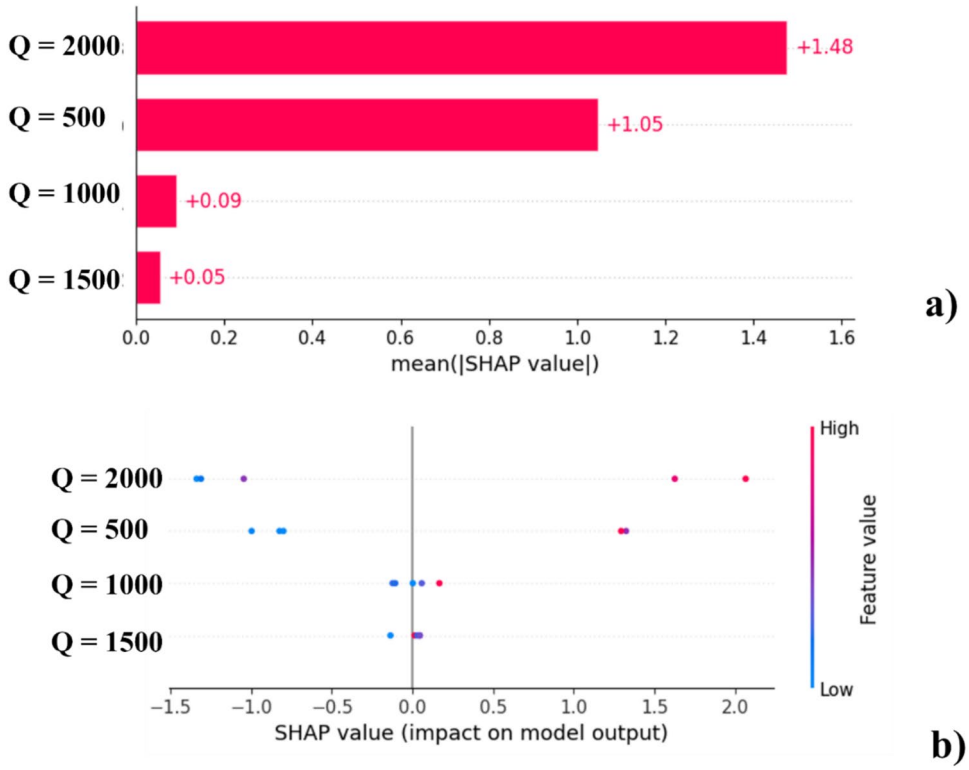


Fig. 20. The impact of (**a**) mean (SHAP values) and (**b**) scatter plot for different heat flux (Q) using Nusselt number

are systematically analyzed. The principal findings, engineering implications, limitations, and future research directions are summarized as follows.

Among the five PCMs investigated, RT-27 exhibited the slowest melting rate, whereas RT-25 achieved complete melting within approximately 1500 s, with an 85.1% higher liquid fraction than RT-27 under identical conditions. Aluminum fins demonstrated the best thermal performance, providing liquid fractions 9.61% and 23.72% higher than those obtained with copper and steel fins. The heptahedral enclosure consistently delivered the best thermal performance. At $t = 1500$ s (RT-27, $\alpha = 0°$, $Q = 1000$ W/m^2), it achieved a liquid fraction of 0.232, representing improvements of 34.88% and 3.13% compared with the rectangular and trapezoidal enclosures, respectively. Additionally, the melting completion time is reduced by 20.4%, while the average heat transfer coefficient increased by 27.6% and 6.7% relative to the rectangular and trapezoidal configurations. Increasing the inclination angle enhanced melting performance with $\alpha = 90°$ producing a 16.6% higher liquid fraction than $\alpha = 30°$. Increasing the heat flux from 500 to 2000 W/m^2 considerably accelerated the melting process, reducing the Fourier number required for complete melting by 77.56%. The Nusselt number increased from approximately 10 to 39, corresponding to a 28.8% enhancement in convective heat transfer. The Random Forest (RF) model accurately predicted the Nusselt number, achieving R^2 values of 0.9896 and 0.9729 for the training and testing datasets with MAPE values below 4%. These results confirm that the RF model provides rapid and reliable predictions of thermal performance.

From an engineering implication, the heptahedral enclosure with aluminum fins, near vertical inclination (70° and 90°), and heat fluxes between 1500 and 2000 W/m^2 is recommended for efficient latent heat thermal energy storage applications. The developed RF model also offers a computationally efficient surrogate for real-time performance prediction and design optimization. The present study is limited by the use of a two-dimensional model, constant thermophysical properties, a single fin configuration, and the lack of experimental validation. Future work should focus on three-dimensional simulations, multi-objective optimization, advanced fin configurations, long-term thermal cycling, and the integration of the surrogate model with real-time control systems. Investigations involving emerging PCM formulations, including shape-stabilized and nano-enhanced PCMs, are also recommended to further improve thermal energy storage performance.

Data availability

All data generated or analysed during this study are included in this published article.

Received: 22 May 2026; Accepted: 20 August 2026
Published online: 05 September 2026

References

1. Liu, D. et al. Numerical evaluation of convective heat transfer properties of two-dimensional rotating PCM melt in the unilaterally heated rectangular container. *Renew. Energy* **193**, 920–940. https://doi.org/10.1016/j.renene.2022.05.009 (2022).
2. Liu, H.-Y., Zhang, L., Wu, C.-M. & Li, Y.-R. Comprehensive investigation of a novel latent energy storage unit exhibiting enhanced natural convection. *Int. J. Heat Mass Transf.* **219**, 124911. https://doi.org/10.1016/j.ijheatmasstransfer.2023.124911 (2024).
3. Kiyak, B., Oztop, H. F., Biswas, N. & Selimefendigil, F. Effects of geometrical configurations on melting and solidification processes in phase change materials. *Appl. Therm. Eng.* **258**, 124726. https://doi.org/10.1016/j.applthermaleng.2024.124726 (2025).
4. Liu, H.-Y., Hu, Y.-P., Yang, G.-Y., Wu, C.-M. & Li, Y.-R. PCM melting characteristics in a sidewall-heated rectangular cavity with non-uniform longitudinal fins near the bottom. *Renew. Energy* **242**, 122451. https://doi.org/10.1016/j.renene.2025.122451 (2025).
5. Zhao, C., Wang, J., Sun, Y., He, S. & Hooman, K. Fin design optimization to enhance PCM melting rate inside a rectangular enclosure. *Appl. Energy* **321**, 119368. https://doi.org/10.1016/j.apenergy.2022.119368 (2022).
6. DeCésaroOliveski, R., Becker, F., Rocha, L. A. O., Biserni, C. & Eberhardt, G. E. S. Design of fin structures for phase change material (PCM) melting process in rectangular cavities. *J. Energy Storage* **35**, 102337. https://doi.org/10.1016/j.est.2021.102337 (2021).
7. Kadhim, S. A. et al. Enhancing the melting rate of RT42 paraffin wax in a square cell with varied copper fin lengths and orientations: a numerical simulation. *Int. J. Thermofluids* **24**, 100877. https://doi.org/10.1016/j.ijft.2024.100877 (2024).
8. Chen, H.-T., Zhang, R.-X., Yan, W.-M., Amani, M. & Ochodek, T. Numerical and experimental study of inverse natural convection heat transfer for heat sink in a cavity with phase change material. *Int. J. Heat Mass Transf.* **224**, 125333. https://doi.org/10.1016/j.ijheatmasstransfer.2024.125333 (2024).
9. Hu, Z., Jiang, S., Sun, Z. & Li, J. Numerical simulation of fin arrangements on the melting process of PCM in a rectangular unit. *Renew. Energy* **220**, 119677. https://doi.org/10.1016/j.renene.2023.119677 (2024).
10. Elsayed, A. O. Numerical investigation on PCM melting in triangular cylinders. *Alex. Eng. J.* **57**(4), 2819–2828. https://doi.org/10.1016/j.aej.2018.01.005 (2018).
11. Hong, Y. et al. Energy storage and heat transfer characteristics of multiple phase change materials in a rectangular cavity with different layouts of T-shaped fins. *Int. Commun. Heat Mass Transf.* **159**, 108068. https://doi.org/10.1016/j.icheatmasstransfer.2024.108068 (2024).
12. Qasem, N. A. A. et al. Investigation of phase change heat transfer in a rectangular case as function of fin placement for solar applications. *Case Stud. Therm. Eng.* **54**, 103996. https://doi.org/10.1016/j.csite.2024.103996 (2024).
13. Kıyak, B., Öztop, H. F., Biswas, N., Coşanay, H. & Selimefendigil, F. Effects of fin shapes and orientations with cyclic heating and cooling on melting and solidification of PCM-filled closed space. *Int. J. Heat Fluid Flow* **112**, 109753. https://doi.org/10.1016/j.ijheatfluidflow.2025.109753 (2025).
14. Czerwiński, G. & Wołoszyn, J. Partitions influence on rectangular latent heat thermal energy storage unit performance during melting and solidification. *Int. Commun. Heat Mass Transf.* **159**, 108047. https://doi.org/10.1016/j.icheatmasstransfer.2024.108047 (2024).
15. L. Tan, Y. Kwok, A. Date, A. Akbarzadeh (2011) Numerical analysis of natural convection effects in latent heat storage using different fin shapes.
16. Zhao, Z., Hu, B., He, J., Lin, M. & Ke, H. Effect of fin shapes on flow boiling heat transfer with staggered fin arrays in a heat sink. *Appl. Therm. Eng.* **225**, 120179. https://doi.org/10.1016/j.applthermaleng.2023.120179 (2023).
17. Hammoodi, K. A. et al. Investigation of the influence of the air layer on the phase change material melting process inside a hemicylindrical enclosure: a numerical approach. *Results Eng.* **24**, 103337. https://doi.org/10.1016/j.rineng.2024.103337 (2024).
18. Barthwal, M. & Rakshit, D. No fins attached? Numerical analysis of internal–external fins coupled PCM melting for solar applications. *Appl. Therm. Eng.* **215**, 118911. https://doi.org/10.1016/j.applthermaleng.2022.118911 (2022).
19. Rawat, P., Ashwni, & Sherwani, A. F. A numerical study on the impact of fin length arrangement and material on the melting of PCM in a rectangular enclosure. *Int. J. Heat Mass Transf.* **205**, 123932. https://doi.org/10.1016/j.ijheatmasstransfer.2023.123932 (2023).
20. Rashid, F. L. et al. Heat transfer enhancement of phase change materials using letters-shaped fins: a review. *Int. Commun. Heat Mass Transf.* **159, Part B**, 108096. https://doi.org/10.1016/j.icheatmasstransfer.2024.108096 (2024).
21. Shen, S., Wu, C. & Duan, F. Machine learning for predicting the PCM melting process in a rectangular enclosure energy storage. *AI Therm. Fluids* **1**, 100001. https://doi.org/10.1016/j.aitf.2024.100001 (2025).
22. Kiaghadi, M., Keshvarinia, M., Boora, F. M. & Mousavi, S. M. Machine learning applications for predicting liquid fraction in a PV system with NEPCM and fins. *Case Stud. Therm. Eng.* **61**, 104819. https://doi.org/10.1016/j.csite.2024.104819 (2024).
23. Abdellatif, H. E., Khan, S. A., Belaadi, A. & Ghernaout, D. Enhancing thermal energy storage: The impact of inclined enclosure geometry and artificial neural network based modeling on phase change material melting performance. *J. Energy Storage* **114, Part A**, 115750. https://doi.org/10.1016/j.est.2025.115750 (2025).
24. Kıyak, B., Öztop, H. F., Ertam, F. & Aksoy, İG. An intelligent approach to investigate the effects of container orientation for PCM melting based on an XGBoost regression model. *Eng. Anal. Bound. Elem.* **161**, 202–213. https://doi.org/10.1016/j.enganabound.2024.01.018 (2024).
25. Tavakoli, A., Hashemi, J., Najafian, M. & Ebrahimi, A. Physics-based modelling and data-driven optimisation of a latent heat thermal energy storage system with corrugated fins. *Renew. Energy* **217**, 119200. https://doi.org/10.1016/j.renene.2023.119200 (2023).
26. Junaid, M., Saha, G., Shahrear, P. & Saha, S. C. Phase change material performance in chamfered dual enclosures: exploring the roles of geometry, inclination angles and heat flux. *Int. J. Thermofluids* **24**, 100919. https://doi.org/10.1016/j.ijft.2024.100919 (2024).
27. Silva Junior, L. G., Ribeiro, G. B. & Mancin, S. Effect of fin configuration on the early stage of the melting process of a phase change material. *Int. J. Thermofluids* **24**, 100957. https://doi.org/10.1016/j.ijft.2024.100957 (2024).
28. Li, C. Melting process of RT-25 as a phase change material by placing innovative rectangular and parallelogram fins: Effect of shape and angle of fins. *J. Energy Storage*, (2023).
29. Tabassum, T., Hasan., M. & Begum, L. 2-D numerical investigation of melting of an impure PCM in the arbitrary-shaped annuli. *Int. J. Therm. Sci.* **114**, 296–319. https://doi.org/10.1016/j.ijthermalsci.2017.01.006 (2017).
30. Ji, C., Qin, Z., Dubey, S., Choo, F. H. & Duan, F. Simulation on PCM melting enhancement with double-fin length arrangements in a rectangular enclosure induced by natural convection. *Int. J. Heat. Mass. Transf.* **127**, 255–265. https://doi.org/10.1016/j.ijheatmasstransfer.2018.07.118 (2018).
31. Qin, H., Wang, Z., Heng, W., Liu, Z. & Li, P. Numerical study of melting and heat transfer of PCM in a rectangular cavity with bilateral flow boundary conditions. *Case Stud. Therm. Eng.* **27**, 101183. https://doi.org/10.1016/j.csite.2021.101183 (2021).
32. Sudsuansee, T. et al. Impact of surface roughness on CFD performance prediction of francis turbines: grid convergence analysis and experimental validation across variable operating conditions. *Int. J. Thermofluids* **32**, 101567. https://doi.org/10.1016/j.ijft.2026.101567 (2026).
33. Alhejaili, W., Pandey, P. & Aly, A. M. Incompressible smoothed particle hydrodynamics simulations enhanced by hybrid artificial intelligence for investigating magnetic field influence on double diffusion in an arc. *Heat Transf. Part Appl. Int. J. Comput. Methodol* https://doi.org/10.1080/10407782.2024.2363500 (2025).
34. Surendar, R. & Pandey, P. Neural network analysis of Soret effect on rotating fluid between parallel plates with magnetohydrodynamic over porous media. *Heat Transf.* **55**(2), 1328–1348. https://doi.org/10.1002/htj.70140 (2026).

35. Sangeetha, S. & Pandey, P. Hybrid nanofluid-assisted enhanced oil recovery: a combined numerical and artificial neural network approach for prediction and optimization. *J. Therm. Anal. Calorim.* **151**(1), 719–732. https://doi.org/10.1007/s10973-025-15006-w (2026).
36. Tian, L.-L., Liu, X., Chen, S. & Shen, Z.-G. Effect of fin material on PCM melting in a rectangular enclosure. *Appl. Therm. Eng.* **167**, 114764. https://doi.org/10.1016/j.applthermaleng.2019.114764 (2020).

Author contributions

S. Anitha: Development of methodology and Writing—Review and Editing. M. Ramanipriya: Writing—Original Draft and Formulation. Iskander Tlili: Writing—Review and Editing. M. R, I. T and S. A contribute equally.

Funding

The authors declare that no funding is received for the research and preparation of this paper.

Competing interests

The authors declare that they have no known competing financial interests or personal relationships that could have appeared to influence the work reported in this paper.

Additional information

Correspondence and requests for materials should be addressed to I.T.

Reprints and permissions information is available at www.nature.com/reprints.

Publisher's note Springer Nature remains neutral with regard to jurisdictional claims in published maps and institutional affiliations.

Open Access This article is licensed under a Creative Commons Attribution-NonCommercial-NoDerivatives 4.0 International License, which permits any non-commercial use, sharing, distribution and reproduction in any medium or format, as long as you give appropriate credit to the original author(s) and the source, provide a link to the Creative Commons licence, and indicate if you modified the licensed material. You do not have permission under this licence to share adapted material derived from this article or parts of it. The images or other third party material in this article are included in the article's Creative Commons licence, unless indicated otherwise in a credit line to the material. If material is not included in the article's Creative Commons licence and your intended use is not permitted by statutory regulation or exceeds the permitted use, you will need to obtain permission directly from the copyright holder. To view a copy of this licence, visit http://creativecommons.org/licenses/by-nc-nd/4.0/.

© The Author(s) 2026